Dong Liu, Casimir Togbé, Luc-Sy Tran, Daniel Felsmann, Patrick Oßwald, Patrick Nau, Julia Koppmann, Alexander Lackner, Pierre-Alexandre Glaude, Baptiste Sirjean, René Fournet, Frédérique Battin-Leclerc and Katharina Kohse-Höinghaus, *Combustion chemistry and flame structure of furan group biofuels using molecular-beam mass spectrometry and gas chromatography – Part I: Furan*, Combustion and Flame, **161** (2014) 748-765.

Combustion chemistry and flame structure of furan group biofuels using molecular-beam mass spectrometry and gas chromatography – Part I: Furan

Dong Liu[1], Casimir Togbé[1], Luc-Sy Tran[2], Daniel Felsmann[1], Patrick Oßwald[1#], Patrick Nau[1], Julia Koppmann[1], Alexander Lackner[1], Pierre-Alexandre Glaude[2], Baptiste Sirjean[2], René Fournet[2], Frédérique Battin-Leclerc[2*], Katharina Kohse-Höinghaus[1*]

[1] Department of Chemistry, Bielefeld University, Universitätsstraße 25, D-33615 Bielefeld, Germany

[2] Laboratoire Réactions et Génie des Procédés (LRGP), CNRS, Université de Lorraine, ENSIC, 1 rue Grandville, BP 20451, 54001 Nancy Cedex, France

[#] now at German Aerospace Center (DLR), Institute of Combustion Technology, Pfaffenwaldring 38-40, D-70569 Stuttgart, Germany

Supplemental Material is available.

[*] Corresponding authors. Katharina Kohse-Höinghaus: E-mail: kkh@uni-bielefeld.de, Phone: +49 521 106 2052, Fax: +49 521 106 6027 and Frédérique Battin-Leclerc: E-mail: Frederique.Battin-Leclerc@univ-lorraine.fr, Phone: +33 3 83 17 51 25, Fax: +33 3 83 37 81 20

Abstract

Fuels of the furan family, i.e. furan itself, 2-methylfuran (MF), and 2,5-dimethylfuran (DMF) are being proposed as alternatives to hydrocarbon fuels and are potentially accessible from cellulosic biomass. While some experiments and modeling results are becoming available for each of these fuels, a comprehensive experimental and modeling analysis of the three fuels under the same conditions, simulated using the same chemical reaction model, has – to the best of our knowledge – not been attempted before. The present series of three papers, detailing the results obtained in flat flames for each of the three fuels separately, reports experimental data and explores their combustion chemistry using kinetic modeling. The first part of this series focuses on the chemistry of low-pressure furan flames. Two laminar premixed low-pressure (20 and 40 mbar) flat argon-diluted (50%) flames of furan were studied at two equivalence ratios (ϕ=1.0 and 1.7) using an analytical combination of high-resolution electron-ionization molecular-beam mass spectrometry (EI-MBMS) in Bielefeld and gas chromatography (GC) in Nancy. The time-of-flight MBMS with its high mass resolution enables the detection of both stable and reactive species, while the gas chromatograph permits the separation of isomers. Mole fractions of reactants, products, and stable and radical intermediates were measured as a function of the distance to the burner. A single kinetic model was used to predict the flame structure of the three fuels: furan (in this paper), 2-methylfuran (in Part II), and 2,5-dimethylfuran (in Part III). A refined sub-mechanism for furan combustion, based on the work of Tian et al. [Combustion and Flame 158 (2011) 756-773] was developed which was then compared to the present experimental results. Overall, the agreement is encouraging. The main reaction pathways involved in furan combustion were delineated computing the rates of formation and consumption of all species. It is seen that the predominant furan consumption pathway is initiated by H-addition on the carbon atom neighboring the O-atom with acetylene as one of the dominant products.

1. Introduction

With tightened fossil fuel resources and rigorous environmental legislation, biofuels are seen as an interesting and promising alternative. Decades of research have been performed to provide chemical databases for the conventional hydrocarbon fuels, but similar information on the richer chemistry of oxygenated and other bio-derived fuels is comparatively recent [1,2]. The so-called "furanics", including furan and its derivatives, are potential biofuels and have significant advantages compared to first-generation biofuels [3-5]. Before a potential biofuel should be used in practice, it is advisable to investigate it carefully with respect to its combustion chemistry, including information on the nature and amount of undesired and potentially harmful products. Some of the earlier experimental studies regarding furan fuels have investigated their thermal decomposition [6-15]. Only a few experiments addressed all three furanic fuels. Especially Grela et al. [6] employed a heated flow reactor to determine the decomposition rates of furan, 2-methylfuran (MF), and 2,5-dimethylfuran (DMF), and analyzed the pyrolysis products using an online gas chromatography coupled to a mass spectrometer at very low pressure (1.3×10^{-3} mbar) and over the temperature range of 1050-1270 K. Also, Lifshitz et al. [7-9] used shock tube experiments to investigate the thermal decomposition of these three furanic fuels over the temperature range of about 1050 to 1460 K, at pressures of 2 atm. Measurements of the final products were also obtained using gas chromatography techniques, and a chemical kinetic mechanism was proposed to model their results. Both Grela et al. [6] and Lifshitz et al. [7-9] concluded that the rate coefficients for thermal decomposition of these furanic fuels increase with increasing alkylation of the furan ring.

Theoretical calculations were also employed to compute the thermal decomposition of furan [16-18]. Liu et al. [16,17] investigated the thermal decomposition of furan using density functional (B3LYP) methods for geometries and QCISD(T) for energies. They reported on the

thermochemistry and energetics of the thermal decomposition channels of furan, but did not give any information about the rate coefficients. Sendt et al. [18] reported the thermochemistry and rate parameters of several key reactions. They also proposed a kinetic mechanism which agrees well with the furan pyrolysis measurements of Organ and Mackie [13]. Sendt et al. [18] also concluded that 1,2-hydrogen atom transfer is the most important pathway for furan consumption in pyrolysis.

Recently, experimental and kinetic investigations of premixed furan flames were reported by Tian et al. [19], using molecular-beam mass spectrometry (MBMS) with synchrotron-based tunable VUV photoionization. A kinetic model was constructed for the prediction of their results. Model calculations were compared with experimental data at 35 Torr (47 mbar) and reasonable agreement was obtained between experiments and predictions. However, there still remains a need for improvement of the mechanism for the combustion of furan. In particular, their model was also not intended to represent the combustion chemistry of alkylated furans.

More recently, Wei et al. [20] measured ignition delay times of furan behind reflected shock waves between 1320 and 1880 K and at 1.2 to 10.4 atm. They modified the chemical kinetic mechanism of Tian et al. [19] to rationalize their results and showed that the model yields reasonable agreement with the experiments. They concluded that the most important fuel consumption path under these conditions is initiated by unimolecular decomposition.

In the present work, as part of a continuing effort to improve the knowledge on the combustion chemistry of furan, MF [21], and DMF [22] we report experimental data of low-pressure premixed furan flames with 50% Ar dilution at two equivalence ratios (ϕ=1.0, C/O=0.40 and ϕ=1.7, C/O=0.64). Two methods of analysis, namely electron-ionization molecular-beam mass spectrometry (EI-MBMS) and gas chromatography (GC) were used. These new experimental results were used to examine the furan mechanism. A kinetic model previously developed for DMF [23] which is based on theoretical calculations [24-26] and

which contains the furan and MF sub-mechanisms was used to simulate the three furanic fuel flames. The furan and MF sub-mechanisms have been completed and improved. Results are also compared to the model of Tian et al. [19]. A detailed reaction flow analysis provides information on the importance of several reaction channels, including those newly added, under the conditions of our experiments.

2. Experiments

The experiments were performed in laminar premixed flat low-pressure flames using EI-MBMS and GC to provide a detailed chemical analysis of stable and reactive species together with isomer identification. EI-MBMS was available in Bielefeld [27-30], whereas online GC was used in Nancy [31].

2.1. Flame conditions

Two flames, stoichiometric ($\phi=1.0$, C/O=0.40) and fuel-rich ($\phi=1.7$, C/O=0.64), were investigated at 20 and 40 mbar, respectively. The flames were stabilized on two similar porous plug burners. Because of a higher adiabatic burning velocity, a lower pressure was used for the stoichiometric flames in order to have a flame front location far enough above the burner surface, thus facilitating the sampling by the probe. The EI-MBMS instrument in Bielefeld is equipped with a home-made bronze-matrix burner of 64 mm diameter, and the burner in Nancy features a commercial bronze McKenna burner of 60 mm diameter. Despite mole fraction values changing with equivalence ratio, the ratio of isomer mole fractions remains usually quite close. Thus, only the fuel-rich flame was studied in Nancy to assist isomer identification. Both burners are mounted on translational stages which can be moved in vertical direction for the burner in Nancy, and in two (vertical and horizontal) directions for that in Bielefeld. The flame

conditions for both experiments are summarized in Table 1; flow rates were adapted to obtain the same gas velocity with respective burner diameters.

In Bielefeld, gas flows were controlled by calibrated mass-flow controllers and liquid furan fuel (>99%) was metered by a syringe pump, evaporated at 373 K, and added to the gas stream. In Nancy, liquid fuel (>98%) was contained in a metallic vessel pressurized with argon. After each load of liquid fuel, argon bubbling and vacuum pumping were performed in order to remove oxygen traces dissolved in the liquid fuel. The liquid fuel flow rate was controlled by a liquid mass-flow controller with an uncertainty of ~0.5%, mixed with argon, and then evaporated by passing it through a Bronkhorst CEM (Controlled Evaporator and Mixer). The temperature of this CEM was set at 373 K. Both burners were cooled with water at a constant temperature of 333 K.

2.2.   Molecular-beam mass spectrometry measurements (Bielefeld)

The MBMS system was described in [27-30]. The EI-MBMS setup consists of a two-stage Wiley-McLaren ion source combined with a reflectron time-of-flight (TOF) detection unit with high mass resolution ($m/\Delta m$=4000). This mass resolution is sufficient to determine the elemental composition of C/H/O species. Samples were extracted from the flame with a quartz cone with a 320 μm diameter orifice at the tip and an angle of 25°.

In the EI-MBMS experiment, the sample was ionized using five different nominal energies (10.5, 11.25, 12, 16.5, and 17 eV) to analyze the flame and minimize fragmentation. A multichannel plate (MCP) serves as detection unit, with a multichannel scaler for data recording. Centerline species profiles were measured as a function of distance from the burner h in so-called "burner scans".

2.3.   EI-MBMS data evaluation

The evaluation of the molecular-beam experiment follows routines previously reported in Refs. [27-30]. Mole fractions of major species were determined based on the elemental balances of carbon, hydrogen and oxygen. At the highest distance from the burner, the products are considered to be CO, CO_2, H_2, and H_2O for ϕ=1.7, while we also consider O_2 at this position for equivalence ratio ϕ=1.0. The mole fractions of these major species can be calculated in the exhaust gas from the measured ratios of CO/CO_2 using the respective element balances for both stoichiometries. The resulting mole fractions are then used to gain calibration factors k_i for product species. Calibration of reactant species was done using the same approach at the burner surface. The error in the mole fractions is estimated to be less than 15% for major species and less than 20% for H_2. Further details on the calibration procedures and on the error estimation can be found in Ref. [30].

The signal $S_i(E)$ of an intermediate species i at the energy E is associated with its partial pressure or its respective mole fraction at the corresponding flame position through the following equation:

$$S_i(E) = p_i \cdot c \cdot SW \cdot D_i \cdot \varphi \cdot FKT(h) \cdot \int \sigma_i(\tau) \cdot f(E - \tau) d\tau \qquad (1)$$

where p_i is the partial pressure of species i (note that p_i is proportional to the mole fraction x_i), c is an instrument factor, SW the number of sweeps, D_i the mass discrimination factor of species i, φ is the number of ionizing particles (photons or electrons), $FKT(h)$ a temperature- and thus position-dependent sampling function, $\sigma_i(E)$ is the ionization cross section of species i at the energy E, τ is the integration variable, and $f(E-\tau)$ is the energy distribution of the ionizing particles. The energy distribution of the electrons (FWHM~1 eV) for the setup in this study is well characterized. The high-energy tail of the distribution permitted the detection of argon with a sufficient signal-to-noise ratio in all measurements, even when the nominal ionization energy was below its ionization threshold (IE=15.759 eV [32]). Argon was thus used as

reference. All signals were normalized by the argon signal at all energies. Eq. (1) then simplifies to:

$$\frac{S_i(E)}{S_{Ar}(E)} = \frac{x_i}{x_{Ar}} \cdot \frac{D_i}{D_{Ar}} \cdot \frac{\int \sigma_i(\tau) \cdot f(E-\tau)d\tau}{\int \sigma_{Ar}(\tau) \cdot f(E-\tau)d\tau} = \frac{x_i}{x_{Ar}} \cdot k_i(E) \qquad (2)$$

where $k_i(E)$ is the species- and energy-dependent calibration factor. With this normalization, all parameters can be condensed into a calibration factor $k_i(E)$. As soon as this factor $k_i(E)$ is determined for a given energy E, the mole fraction x_i of an intermediate species can be calculated based on the argon mole-fraction profile from the major species calculation.

Calibration factors k_i for intermediate species can be obtained by direct cold-gas calibration measurements whenever stable gaseous cold-gas mixtures are feasible. In all other cases, calibration factors were estimated either using the relative ionization cross section method (RICS) [33] or the convolution of the literature ionization cross sections with the known energy distribution of the ionizing electrons [29]. Further information on both methods can be found in Ref. [30]. To avoid fragmentation, the scan with the lowest possible energy was used for each species. Typically good agreement of species profiles for different electron energies was noted. The respective calibration method, electron energy, and literature ionization threshold for each species are listed in Table 2.

The accuracy of the experimental results depends predominantly on the quality of the available calibration data including quality of ionization cross sections, fragmentation patterns, and calibration methods for the respective species. Typical error limits from a large number of flame studies with different experiments may be estimated as follows. For directly calibrated species, the error is below 30%; the uncertainty associated with the convolution procedure depends on the quality of the literature ionization cross section (typical uncertainty below a factor of 2). For radicals for which the RICS procedure was used, the error is estimated to be in the range of factors of 2-4. Each species mole fraction exhibits an individual absolute

9

uncertainty. The error is, however, identical for all measured flames and a relative comparison of trends between the flames can thus be performed with significantly higher precision.

2.4. Gas chromatography measurements (Nancy)

The experimental setup has been developed in LRGP (Nancy) to study stable species profiles in a laminar premixed flat flame at low-pressure and has been described previously [31]. Briefly, analyses were made by GC with a heated (at 423 K) online connection to a quartz probe. The quartz probe had an upper diameter of 6 mm and was tipped by a small cone with a 100 μm diameter orifice at the tip and an angle to the vertical of 20°. Three types of columns were used: Carbosphere, HP-Plot Q, and HP-Molsieve, and two types of detectors: flame ionization detection (FID) coupled with a methanizer and thermal conductivity detection (TCD). The Carbosphere column with argon as carrier gas was used to analyze O_2 and H_2 by TCD. The HP-Plot Q column with helium as carrier gas was used to analyze all the hydrocarbon species from C_2 and oxygenated species by FID. Additionally, this column was used also to analyze H_2O by TCD. The HP-Molsieve column with helium as the carrier gas was used to analyze CH_4 and C_2H_4 by FID and Ar by TCD. In usual gas chromatography, CO and CO_2 can only be detected by TCD. Here, CO and CO_2 were passed through the methanizer, were converted to methane, and could then be detected by FID which is more sensitive (by a factor of 100) than TCD. Stable species were identified by the determination of their individual retention times and by mass spectrometry (GC/MS). Calibrations were made directly using cold-gas mixtures. The calibration factors were estimated using the effective carbon number (ECN) method for species for which a direct calibration procedure is not applicable. The calculated uncertainties of the mole fraction measurements of the quantified species were ~5% for the major compounds and ~10% for minor products (<100 ppm). The FID detection threshold was about 1 ppm, while the TCD detection limit was about 50 ppm for H_2O, H_2 and O_2.

2.5.   Temperature measurements

The temperature profile is an important input for the successful kinetic modeling of one-dimensional flames, and it was determined according to the procedures described in [29,30]. In this study, the temperature profiles (measured only in Bielefeld) for the flame simulation were calculated based on the temperature dependence of the sampling rate through the probe orifice to account for the distortion caused by the sampling cone. Assuming a constant pumping speed, the gas flow rate through the sampling orifice can be expressed by the pressure of the first-stage chamber (p_{1st}). This dependence is given by:

$$p_{1st} = C\sqrt{\frac{\gamma}{\overline{M}T}} \cdot \left(\frac{2}{\gamma+1}\right)^Z \tag{3}$$

with $Z = (\gamma + 1)/2(\gamma - 1)$. $\overline{M}$ is the mean molar mass, γ is the adiabaticity coefficient (C_p/C_v), close to unity and therefore set equal to 1, and C is a temperature-independent device-specific constant. This apparatus constant C was determined by solving Eq. (3) using the exhaust gas temperature taken from the undisturbed temperature measurement by a pulsed quantum cascade laser (QCL). The temperature profiles are used as input parameters in the flame model simulations without any shift between measurement and computation.

Concerning the determination of the exhaust gas temperature, mid-infrared absorption spectroscopy of CO and CO_2 was applied using a pulsed quantum cascade laser (Cascade Technologies) at 4.48 µm. During the 500 ns long laser pulses the wavelength was scanned over ~2 cm^{-1}. The laser beam was focused into the center of the burner with a lens (f=+500 mm) to achieve a spatial resolution of 0.4 mm. Behind the burner chamber the laser pulse was detected with a fast detector (VIGO Systems, PVI-2TE-8) and digitized with a fast digitizer (Agilent U1071A, 500 MHz, 2 GS/s). A pulse repetition frequency of 20 kHz was used, and 20000 individual laser pulses were averaged to increase the signal-to-noise ratio. Wavelength calibration was performed with a Ge-Etalon (FSR=0.048 cm^{-1}). To obtain the absorption

spectrum in the center of the flame, tomographic reconstruction was used [34,35]. For this purpose the burner was moved by steps of 1.5 mm laterally from the center of the flame. The temperature was obtained by fitting the absorption spectrum of CO and CO_2 between 2231.39 and 2232.00 cm^{-1} using the line positions and line strengths from the HITEMP database [36]. The resulting temperature profiles, which have been used in the predictions, are included in Fig. 1. This calibration temperature was measured at 25 mm and the error is estimated to be ~5%.

3. Experimental results

In this study, more than 50 species, including reactants, products, stable intermediates and radical species, were detected and identified. In the following, we concentrate on reporting important examples from the experimental perspective and highlight some aspects of mole fraction profiles for some species, presented in Figs. 1-10. Comparison with modeling results is given in Section 5.

Figures 1-8 report results obtained using EI-MBMS. The GC measurements focused on the identification of isomers, examples for which can be found in Figs. 9 and 10. Figure 1 shows the major species profiles including the temperature profile. The open symbols at 43 mm are equilibrium values calculated with Gaseq [37] for the measured peak temperatures. The mole fractions of these major species at h=40 mm are close to equilibrium values, especially in the fuel-rich flame. The discrepancies observed between experimental results and the equilibrium values are within ~20%. The reaction zones of both flames are located approximately 2 and 4 mm above the burner, evident also from the intermediate species profiles in Figs. 2-8. Note that the flame is closer to the burner in the GC experiment and that the conditions for the two setups are not exactly identical (especially regarding the size of sampling probes); thus the temperature profiles are different and the species profiles obtained by GC and MBMS are

shifted (as shown in Figs. 9 and 10). Nevertheless, the comparison between maximum mole fractions measured by both analysis methods is reported in Table 3.

Figure 2 presents methyl radical (CH_3) and methane (CH_4) mole fraction profiles with maxima of ~2-3×10^{-3} near 3 mm for the latter species. In Fig. 3, the profiles of the C_2 species acetylene (C_2H_2), ethene (ethylene, C_2H_4), ethyl radical (C_2H_5), and ethane (C_2H_6) are given for ϕ=1.0 and 1.7. They reach their maxima ~2.5 mm above the burner. Acetylene is the most abundant species of this series with peak mole fractions of 1.8×10^{-2} (ϕ=1.0) and 3.5×10^{-2} (ϕ=1.7).

Figure 4 presents the profiles of the C_3 products, with sum of allene and propyne (C_3H_4), allyl radical (C_3H_5) and propene (C_3H_6). C_3H_4 is the most abundant C_3 species with peak mole fractions of 1.8×10^{-3} (ϕ=1.0) and 3.0×10^{-3} (ϕ=1.7). Isomers of C_3H_4 are not distinguishable in the EI-MBMS experiment, but were identified separately with the GC analysis. Figure 9 thus provides the mole fraction profiles of total C_3H_4 (EI-MBMS), and the isomers of C_3H_4 from the GC analysis (sum of C_3H_4, allene, and propyne). This figure shows that propyne is the most abundant species of the two isomers of C_3H_4. Note that the experimental MBMS mole fractions are relatively high since the total MBMS signal was calibrated as propyne.

Figure 5 presents the profiles of the observed C_4 species. C_4H_8 (sum of 1-butene and 2-butene) is produced first and peaks near h=2 mm with mole fractions of 5.1×10^{-4} (ϕ=1.0) and 6.4×10^{-4} (ϕ=1.7). The profiles of C_4H_2 (1,3-butadiyne), C_4H_4 (1-butene-3-yne), and C_4H_6 (sum of 1,3-butadiene, 1,2-butadiene, and 2-butyne) reach their maxima near 3 mm. The mole fraction profiles of total C_4H_8 (EI-MBMS), and the respective isomers of C_4H_8 from the GC analysis are also presented in Figure 9. From the GC analysis, C_4H_8 is for a large part 1-butene, and C_4H_6 is predominantly 1,3-butadiene. In the GC measurement, the most abundant C_4 species is 1-butene-3-yne (or vinylacetylene, C_4H_4, see Table 3). The small secondary peak

seen in the MBMS experiment for C_4H_8 (Figs. 5 and 9) as well as for C_3H_6O (Figs. 8 and 10) is probably an experimental artefact.

Figure 6 shows the mole fraction profiles of C_5 and C_6 compounds which are formed in low amounts. C_5H_6 (sum of 1,3-cyclopentadiene and 1-pentene-3-yne), C_6H_2 (1,3,5-hexatriyne), and C_6H_6 (benzene) reach their maxima near $h=3$ mm. The most abundant one is benzene with a peak mole fraction of 1.3×10^{-4} ($\phi=1.7$).

Figures 7 and 8 present the mole fraction profiles of selected oxygenated intermediates. C_2H_4O (mostly acetaldehyde) peaks first near 2 mm with a maximum mole fraction of 3.2×10^{-3} ($\phi=1.7$). CH_2O (formaldehyde) and C_2H_2O (ketene) peak further in the flame near 3 mm with maximum mole fractions of $\sim 3.8 \times 10^{-3}$ and $\sim 3.6 \times 10^{-4}$ ($\phi=1.7$), respectively. C_2H_6O (dimethylether) is found in lower amounts with maximum mole fractions of 2.4×10^{-5} and 3.9×10^{-5} in the stoichiometric and fuel-rich flame, respectively (Fig. 7). The profile of the toxic compound propenal (acrolein, C_3H_4O) peaks near 2.5 mm with an appreciable peak mole fraction of 2.8×10^{-3} in the stoichiometric flame and near 2.0 mm with a peak mole fraction of 2.4×10^{-3} in the fuel-rich flame (Fig. 8). Acrolein, acetaldehyde, and formaldehyde are thus the most abundant species of this category. C_3H_6O (propanal and acetone) peaks near 2.0 mm with the maximum mole fraction being approximately doubled with decreasing equivalence ratio from 1.7 to 1.0. The isomer composition for C_3H_6O is given in Fig. 10, showing that propanal is the most abundant isomer of C_3H_6O. The formation of higher-mass oxygenated compounds, such as of phenol (C_6H_6O) and DMF (C_6H_8O), is low with peak mole fractions below 10^{-5} (see Table 2).

Concerning aromatic species, which are well known as soot precursors, benzene was detected with a maximum mole fraction of 4.2×10^{-5} and 1.3×10^{-4} in the stoichiometric and fuel-rich flame, respectively, while toluene and phenol were measured with a smaller mole fraction (lower than 10^{-5}, see Table 2). Two other aromatic compounds including styrene (C_8H_8) and

ethyl benzene (C_8H_{10}) were detected by GC, but their mole fractions are also $<10^{-5}$. In the EI-MBMS measurements, species with a nominal mass $m/z > 96$ were not evaluated because their signals were very small.

In comparison with the work of Tian et al. [19], some species were identified in both studies, e.g. propyne, allene (C_3H_4), 1-butene-3-yne (vinylacetylene, C_4H_4), 1,3-cyclopentadiene (C_5H_6), benzene (C_6H_6), toluene (C_7H_8), acetaldehyde (C_2H_4O), acrolein (C_3H_4O), and 2-methylfuran (C_5H_6O). However, several species are well detected in the present study (Table 3), but were not found in the measurement of Tian et al. [19], such as C_2H_6 (ethane), C_3H_6 (propene), C_4H_8 (1-butene and 2-butene), C_5H_{10} (2-pentene, 3-methyl-1-butene, and 1-pentene), C_2H_6O (dimethylether), C_4H_6O (2-butenal, 2-butenone, isobutenal, and 2,3-dihydrofuran), and C_4H_8O (isobutanal and 2-butanone). Note that a general good agreement between EI-MBMS and GC measurements (see Table 3) is observed for the maximum mole fraction of these species, within the experimental error limits.

4. Kinetic modeling

The kinetic modeling of furan combustion was performed using the CHEMKIN package [38]. The premixed flat flame experiments were modeled using the PREMIX code. The inputs to each simulation included a detailed chemical kinetic reaction mechanism with 305 species in 1472 reactions (in CHEMKIN format) and data sets of thermochemical and transport properties. These input files are available in the Supplemental Material.

The reaction mechanism used here is based on a previous mechanism by Sirjean et al. [23] which was developed to describe the combustion of 2,5-dimethylfuran. In this mechanism [23], the furan oxidation sub-mechanism of Tian et al. [19] and an MF oxidation sub-mechanism based on analogies with DMF and furan reactions were already included. Based on the comparison between experimental measurements and modeling in this series of fuel studies

(Part I: furan, Part II: MF, and Part III: DMF), some of the reactions or rate parameters of the furan and MF sub-mechanisms [23] were updated or replaced to improve the simulation of some intermediates. This was done to attempt to develop a comprehensive mechanism for all three fuels, while the DMF sub-mechanism of Sirjean et al. [23] was not changed.

The detailed chemical kinetic mechanism used in this study is based on a hierarchical nature of combustion mechanisms. The C_0-C_2 sub-mechanism is based on a previous one of Curran and co-workers in its recent version given in [39], with several significant updates based on recent experimental and kinetic data. For species larger than C_2, the reaction base developed in Nancy [40-42] was used. Only the sub-mechanism of furan will be discussed in this work, while those for the two others fuels (MF and DMF) will be presented in Part II [21] and Part III [22], respectively. Low-pressure coefficients were used in the case of pressure-dependent rate coefficients. It is important to note that the high-pressure rate coefficients of Sirjean et al. [23] need to be used for simulation of data under high-pressure conditions.

The most significant modification of the furan oxidation sub-mechanism of Tian et al. [19] is the addition of two missing reaction pathways of consumption of the dihydrofuryl radicals, C_4H_5O-2 and C_4H_5O-3, presented in Fig. 11 (dashed arrows). The $CHCHCH_2CHO$ radical, produced from the C_4H_5O-2 radical by β-scission of the C-O bond, can lead to the CH_2CHCH_2CO radical by 1,4-H transfer (R231) with an activation energy of 6.19 kcal mol^{-1} which is lower than that of reaction $CHCHCH_2CHO=C_2H_2+CH_2CHO$ (24.0 kcal mol^{-1}). Thus, this 1,4-H transfer pathway has been considered in this study and been added to the furan oxidation sub-mechanism. Among the three consumption pathways of C_4H_5O-3, via a resonance-stabilized radical ($CH_2CHCHCHO$), the 1,4-H transfer pathway (R234) requires the lowest activation energy (28.8 kcal mol^{-1}). The 1,4-H transfer of $CH_2CHCHCHO$ leads to the $CH_3CHCHCO$ radical (R234) followed by a subsequent α-scission to form CO and the C_3H_5-s radical (R235). Thus, this decomposition pathway has also been considered in the present study

and been added to the furan oxidation sub-mechanism. The rate coefficients of the reactions R231, R234, and R235 were calculated by means of transition state theory (TST) based on quantum calculations with the CBS-QB3 method [43] implemented in the Gaussian 09 program suite [44] and presented in Table 4.

5. Discussion

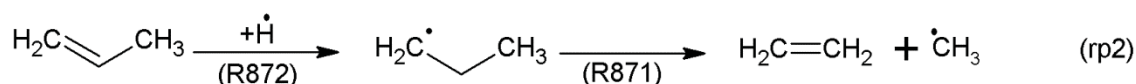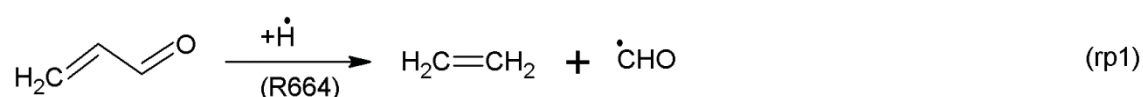### 5.1 Comparison between experimental and simulated results

Simulations were performed using PREMIX software from CHEMKIN [38]. The measured perturbed (with probe) temperature profiles were used as input parameters without any shift between measurement and simulation.

The comparison between experimental and simulated data for the major species in the two furan flames (ϕ=1.0 and 1.7) is shown in Fig. 1. Overall, the model satisfactorily reproduces the consumption of reactants (furan and O_2), the formation of main products (CO_2, CO, H_2O, H_2), and consequently the diluent profiles (Ar). This applies to the profile shapes as well as the mole fractions. Note that small discrepancies between predictions and experiments were observed for mole fractions beyond 10 mm, especially for the H_2O and CO_2 profiles in the stoichiometric flame and only for CO_2 in the fuel-rich flame, but within the experimental error range.

Figures 2-6 display the comparison between experimental and simulated data for the hydrocarbon intermediates in the two furan flames (ϕ=1.0 and 1.7). These figures show that an overall good agreement can be observed, especially for the peak locations and profile shapes. Indeed, the mole fraction profiles of CH_4, C_2H_2, C_2H_5, C_2H_6, and C_3H_6 (for ϕ=1.0) and of C_4H_2, C_4H_4, C_4H_8, C_5H_{10}, C_6H_2, and C_6H_6 (for ϕ=1.7) are well predicted. The model overpredicts the maximum mole fractions of the radicals CH_3 (Fig. 2) and C_3H_5 (Fig. 4), but predicts well their shapes and the peak location. Note that the calibration method used for these

17

two radicals is RICS, from CH_4 for CH_3 and from C_3H_6 for C_3H_5. The typical error of this calibration method is up to a factor of 4 for radicals. Therefore, the agreement can be considered as still within the expected uncertainties for these two radicals. The model, however, is not able to predict some other species within the experimental error limits. These species and potential sources of uncertainties will be discussed below.

The formation of C_2H_4 (Fig. 3) is underpredicted by a factor of 2-3 by the model which is not covered by the experimental uncertainty. However, a good agreement between EI-MBMS and GC measurements (as shown in Table 3) in the fuel-rich furan flame is observed for the maximum mole fraction of C_2H_4. The rate of production (ROP) analysis shows that C_2H_4 is mainly formed from C_2H_3CHO (acrolein, C_3H_4O) and C_3H_6 through the reaction pathways (rp1) and (rp2):

$$H_2C{=}\!\!\diagup\!\!\diagdown{=}O \xrightarrow[\text{(R664)}]{+\dot{H}} H_2C{=}CH_2 \;+\; \dot{C}HO \tag{rp1}$$

$$H_2C{=}\!\!\diagdown\!\!CH_3 \xrightarrow[\text{(R872)}]{+\dot{H}} H_2\dot{C}\!\!\diagdown\!\!CH_3 \xrightarrow[\text{(R871)}]{} H_2C{=}CH_2 \;+\; \dot{C}H_3 \tag{rp2}$$

Via reaction R664, a large part of C_2H_4 is formed from C_2H_3CHO which is a primary species in the decomposition pathways of furan (furan+OH=C_2H_3CHO+CHO). C_2H_4 is also formed from C_3H_6 via the formation of the C_3H_7 radical (R871 and R872). Both C_2H_3CHO and C_3H_6 are overpredicted by the model. Indeed, acrolein (Fig. 8) is slightly overpredicted in the fuel-rich flame and overpredicted by a factor of 2 in the stoichiometric flame. C_3H_6 (Fig. 4) is slightly overpredicted in the stoichiometric flame and overpredicted by a factor of 3 in the fuel-rich flame. These overpredictions could be due to a lack of conversion towards the formation of C_2H_4 within the model.

The formation of C_2H_6 (Fig. 3) is well predicted in the fuel-rich flame, but underpredicted by a factor of 5 in the stoichiometric flame. In the fuel-rich flame, a good agreement between EI-MBMS and GC measurements (see Table 3) is also observed for the maximum mole

fraction value of C_2H_6. In both flames, 100% of C_2H_6 is formed from the combination of two CH_3 radicals: $CH_3+CH_3(+M)=C_2H_6(+M)$, and most of C_2H_6 converts to the C_2H_5 radical by H-abstraction.

The formation of C_3H_4 (Fig. 4), sum of allene ($H_2C=C=CH_2$, aC_3H_4) and propyne ($HC\equiv C-CH_3$, pC_3H_4), is underpredicted by the model (by a factor of 3 in the fuel-rich and of 4 in the stoichiometric flame). aC_3H_4 and pC_3H_4 cannot be distinguished in the EI-MBMS experiment but can be separated in the GC measurements as presented in Fig. 9. The experimental propyne/allene ratio in the GC experiment is ~3.6 (in the fuel-rich flame), while it is ~1.1 (in the fuel-rich flame) and ~0.7 (in the stoichiometric flame) in the simulations. This observation shows a lack of propyne formation in the simulation. According to the ROP analysis result at the maximum simulated mole fraction of pC_3H_4 (h=3mm, T=1658 K; see the simulated profile of pC_3H_4 in Fig. 9), pC_3H_4 is mainly formed by the reaction of C_2H_2 with CH_2 radical and by the decomposition of 1,2-butadienal ($CH_2CCHCHO$). Since the formation of C_2H_2 is well predicted (Fig. 3), the lack of propyne formation could result from the latter reaction. As shown in the reaction sequences below, $CH_2CCHCHO$, which is a primary product from the decomposition of furan, is consumed through the two reaction pathways rp3a (forming pC_3H_4 and CO) and rp3b (forming C_3H_3 and CHO). In Ref. [19], the rate coefficients of the reactions R194 and R249 have been theoretically calculated, while that of reaction R248 was the one proposed by Sendt et al. [18] (for high-pressure limit) with the A-factor divided by 2.2 because of the pressure effect. Note that the temperature dependence constant n of these reactions should significantly change with pressure regarding those of R194 (n=0.416 at high-pressure limit, n=-13.388 at 4.7 kPa) and R249 (n=0.419 at high-pressure limit, n=-15.352 at 4.7 kPa) [19]. However, that of reaction R248 has been kept the same for both low- and high-pressure limits (n=0). Therefore, at low pressure and high temperature (T=1658 K for example), the reaction R248 becomes faster than R249, and therefore hinder the formation of

pC$_3$H$_4$ through R249. Indeed, at the maximum mole fraction of pC$_3$H$_4$ (h=3mm, T=1658 K), only ~30% of CH$_2$CCHCHO decomposes to pC$_3$H$_4$+CO (R249), while ~70% converts to C$_3$H$_3$+CHO (R248). Note that reaction R248 contributes only ~15% to the formation of C$_3$H$_3$ radical. From the discussion above, it can be noted that, at low pressure and high temperature, uncertainty in the rate coefficient of reaction R248 significantly affects the branching ratio of the CH$_2$CCHCHO decomposition (rp3a/rp3b), resulting in a lack of pC$_3$H$_4$ formation. Moreover, this lack could also result from a decrease of the effectiveness of reaction R194 due to a competition of other fuel consumption pathways under these flame conditions.
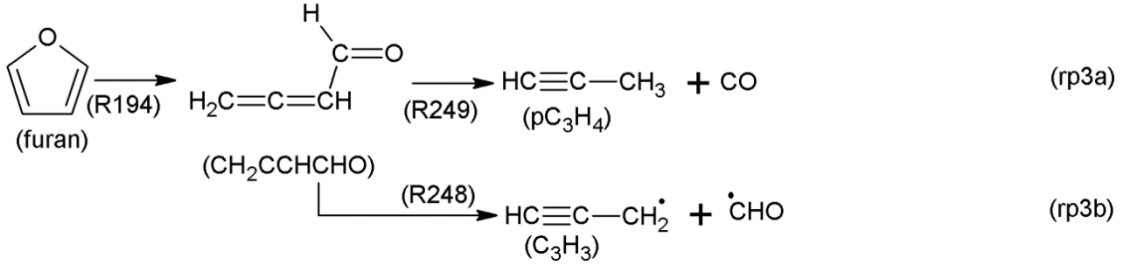
The formation of C$_4$H$_2$ (Fig. 5) is quite well predicted by the model in the fuel-rich flame, but overpredicted by a factor of 3 in the stoichiometric flame. This overprediction is slightly higher than the error limit of the calibration method for C$_4$H$_2$ (below a factor of 2 for method "Convolution"). The ROP analysis shows that ~95% of C$_4$H$_2$ is formed by the reaction C$_2$H$_2$+C$_2$H in the both flames. As C$_2$H$_2$ is well predicted, this disagreement could result from an overprediction of C$_2$H in the stoichiometric flame.

The formation of C$_4$H$_6$ (Fig. 5), sum of 1,3-butadiene (1,3-C$_4$H$_6$), 1,2-butadiene (1,2-C$_4$H$_6$), and 2-butyne (2-C$_4$H$_6$), is underpredicted in both flames. For EI-MBMS, C$_4$H$_6$ is calibrated as 1,3-butadiene which is the most abundant one of the three isomers of C$_4$H$_6$ as shown in Table 3. A good agreement between EI-MBMS and GC measurements (Table 3) is observed for the maximum mole fraction of C$_4$H$_6$. The underprediction for the C$_4$H$_6$ profile results from the underprediction for the formation of 1,3-C$_4$H$_6$. The ROP result indicates that in the fuel-rich flame, most of 1,3-C$_4$H$_6$ is formed from 1-butene (1-C$_4$H$_8$) via the resonance-stabilized C$_4$H$_7$

radical (CH_3-CH-CH=CH_2), while in the stoichiometric flame, only 30% results from this pathway. Here, a large part (~50%) of 1,3-C_4H_6 is formed from the combination of two vinyl radicals (C_2H_3). The C_2H_3 radical is mainly produced from acrolein (C_2H_3CHO) via the formation of the C_2H_3CO radical. As C_4H_8 in the fuel-rich flame (Fig. 5) and C_2H_3CHO in both flames (Fig. 8) are satisfactorily predicted, the disagreement for the C_4H_6 profile could result from a potentially missing third formation pathway of 1,3-C_4H_6 in the model.

The formation of C_5H_6 (Fig. 6) is also underpredicted in both flames. In EI-MBMS, C_5H_6 is calibrated as 1,3-cyclopentadiene (1,3-C_5H_6) which is the most abundant one of the two isomers of C_5H_6 (more than 80%). A good agreement between EI-MBMS and GC measurements (see Table 3) is observed for the maximum mole fraction of C_5H_6. The ROP analysis indicates that most part of 1,3-C_5H_6 is formed directly from the phenoxy radical ($C_6H_5O\#$) or via the formation of the cyclopentadienyl radical ($C_5H_5\#$).

Figures 7 and 8 display the comparison between experimental and simulated data for the oxygenated intermediates in the two furan flames (ϕ=1.0 and 1.7). The measurement shows that the formation of oxygenated intermediates weakly depends on the equivalence ratio (except for C_2H_6O and C_6H_6O), and that the formation of some species, including C_2H_4O and C_3H_6O, is slightly inhibited under fuel-rich conditions. The mole fraction profiles of CH_2O, C_2H_2O, and C_2H_6O (Fig. 7) and of C_3H_4O, C_3H_6O, and C_6H_6O for ϕ=1.7 (Fig. 8) are quite well predicted within the error limits of experimental values. The model tends to underpredict the formation of C_2H_4O (Fig. 7) in both flames.

The mole fraction of C_2H_4O is the sum of that of acetaldehyde (CH_3CHO) and ethylene oxide (CH_2-O-CH_2). As a first approximation, ethenol (CH_2=CH-OH) is ignored in the simulation. In EI-MBMS, C_2H_4O is calibrated as acetaldehyde which is the most abundant one of the isomers of C_2H_4O (see Table 3). A good agreement between EI-MBMS and GC measurements is observed for the maximum mole fraction of C_2H_4O (~3×10^{-3} in the ϕ=1.7

21

flame), but this value is much higher than that in the measurement of Tian et al. [19] for nearly identical conditions (~4×10^{-5} in a ϕ=1.8 flame at 47 mbar). The use of different, independent measurement techniques can thus be a very valuable approach to resolve such discrepancies, especially if additional disagreement between model and experiment is noted. In this study, the underprediction by a factor of 3-4 (Fig. 7) for the C_2H_4O profile results from the underprediction for the formation of acetaldehyde (CH_3CHO). The ROP result indicates that most of acetaldehyde is formed by the reaction $C_3H_5\text{-s}+O_2=CH_3CHO+CHO$ (R751). Note that C_3H_5-s is formed through the following H-addition pathway of furan (rp4):
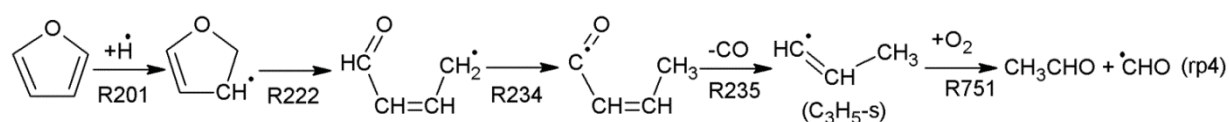
The rate coefficients of reactions R222, R234, and R235 were theoretically calculated, while that of reaction R201 has been estimated by analogy with the values proposed by Gueniche et al. [41] for the similar reaction of 1,3-butadiene and that of reaction R751 has been measured by Slagle et al. [45] in the range T=296-600 K, p=0.13-0.50 kPa (1.3-5.0 mbar). The uncertainties of the rate coefficients of R201 and R751 or a probable missing reaction pathway in the furan sub-mechanism which can form acetaldehyde could potentially explain the underprediction of the formation of CH_3CHO.

Figures 2-8 show that there is a difference between the present simulations and those of Tian et al. [19] (presented as dotted lines). This difference may result partly from the addition of some reaction pathways of furan, see Section 4, as well as from the use of different reaction bases for the C_0-C_2 species. Tian et al. [19] used the reaction base which was developed in LRGP (Nancy), while the model of Sirjean et al. [23] used here involves more recent work, especially the contribution of Curran et al. to the mechanism detailed in [39]. While it is not easy to quantify a potential overall improvement – for some species, the prediction of the Tian et al. mechanism [19] is better, for others, the present one shows a better match to the

experimental data – a significant progress lies in the comprehensive approach used here to model experiments for all three furanic fuels with the same mechanism. Overall, the improvement of our mechanism can be seen in the furan flames of both stoichiometries.

To investigate the effect of the addition of reaction pathways (see Section 4) as well as the use of different reaction bases for C_0-C_2 species, we used our model to simulate the flame structure of Tian et al. [19]. Figures S1-S4 in the Supplemental Material show a comparison of the model simulations with the flame data at equivalence ratios 1.4 and 1.8. The experimental and modeling mole fraction profiles of reactants and main products (Fig. S1) fit quite well, except for the CO and H_2O profiles in the reaction zone and for most main species close to the burner surface. Similar disagreement for CO and H_2O profiles has also appeared in the results of Tian et al. [19]. This disagreement is possibly caused by the uncertainties in the PI-MBMS measurement, because the present model predicted well the formation of these species in our present EI-MBMS data (Fig. 1). A small discrepancy (~17%) between predictions and experiments is also observed for the mole fraction values of H_2O in the exhaust gas zone. The comparison between experimental and simulated data for intermediates (Figs. S2-S4) shows that an overall agreement can be observed within the experimental error range.

5.2 Reaction pathways of furan combustion

Reaction path analyses were performed with the PREMIX software, and the main consumption pathways of furan were identified. The structure and nomenclature of selected species relevant to the following discussion in this section are shown in Table 5. Figure 12 displays the main reactions involved in the consumption of furan and intermediate species in the fuel-rich flame (ϕ=1.7) at a distance of 2.46 mm from the burner, corresponding to a temperature of 1135 K and 71% conversion of furan. A sufficient conversion has been chosen so that the major ways of consumption of the primary products can be observed.

Under these conditions, furan is mainly (73%) consumed by H-addition at the C2 position of furan (the carbon atom bound to the oxygen atom, see Fig. 12) to produce the dihydrofuryl-3 radical (C_4H_5O-3). The second important furan consumption channel (15%) is the OH-addition at the C═C double bond forming acrolein (C_2H_3CHO) and the CHO radical. Minor furan consumption channels are H-abstractions forming furyl-2 and furyl-3 radicals, and H-addition on the C3 position of furan (away from the oxygen atom, see Fig. 12) yielding the dihydrofuryl-2 radical (C_4H_5O-2). The contribution of other channels in the consumption of furan is very small (<1%). Addition of other radicals (such as O and OOH) to a C═C double bond of furan was not included in the model. This is one of the drawbacks of the present model which will need further experimental and theoretical studies. It can be noted, however, that this type of reaction is not favored under high-temperature conditions because the concentrations of O-atoms and OOH radicals are much lower than those of H-atoms and OH radicals, and the rate coefficients of OOH-addition to the double bond are usually much lower than those of H- and OH-additions. Additionally, at this moment no detailed information about these reactions (O- and OOH-addition to the double bond of furan) is available in the literature. For all these reasons, only H- and OH-additions were considered in the model.

Subsequently, the C_4H_5O-3 radical reacts mainly by β-scission of the C-O bond (99%) resulting in the resonance radical $CH_2CHCHCHO$. Most of $CH_2CHCHCHO$ is then consumed by isomerization yielding the $CH_3CHCHCO$ radical (98%), followed quickly by an elimination of CO to form the C_3H_5-s radical. This reaction pathway was added to this study (see Section 4). The C_3H_5-s radical is consumed by β-scission of the C-C bond to produce C_2H_2 and CH_3 and by isomerization to form the allyl radical (C_3H_5-Y).

By β-scission of a C-O bond, the C_4H_5O-2 radical forms the $CHCHCH_2CHO$ radical (99%) which then yields the CH_2CHCH_2CO radical by isomerization (57%) and decomposes to C_2H_2 and the CH_2CHO radical by β-scission of a C-C bond (43%). The first (isomerization) pathway

was added in this study (see Section 4). By α-scission of a C-C bond, the CH_2CHCH_2CO radical quickly decomposes into the C_3H_5-Y radical and CO.

Both furyl-2 and furyl-3 radicals are mainly consumed by β-scission of a C-O bond yielding the CHCHCHCO and CHCCHCHO radicals, respectively. The CHCHCHCO radical is then completely consumed by β-scission of a C-C bond to give C_2H_2 and the CHCO radical. The resonance-stabilized CHCCHCHO radical is mainly consumed by forming CO and the C_3H_3 radical via the formation of $CHCCH_2CHO$ or CO and the C_4H_5-1s radical via the formation of C_5H_6O. The decompositions yielding C_3H_3+CO or H+CH≡CCH=C=O (ethynylketene) are minor channels of the consumption of the CHCCHCHO radical.

The reaction pathways of formation of some species, which have not yet been discussed above, are presented below (but not shown in Fig. 12).

About 83% of C_4H_4 is formed through the reaction C_3H_3+CH_2=C_4H_4+H. Most of 1-butene (1-C_4H_8) results from the reaction of the combination of the C_3H_5-Y and CH_3 radicals (C_3H_5-Y+CH_3=1-C_4H_8), then mainly consumed by H-abstraction to give the C_4H_7 radical (CH_3-CH-CH=CH_2). C_6H_2 is formed through the reaction of 1,3-butadiyne (C_4H_2) and the C_2H radical and then completely consumed to give the same molecules. Benzene (C_6H_6) is mainly produced from the combination of the phenyl radical (C_6H_5) with an H-atom or of two resonance-stabilized propargyl radicals (C_3H_3). Methanol (CH_4O) is mainly formed through the reactions: CH_3O+CH_3O=CH_4O+CH_2O and CH_3+OH(+M)=CH_4O(+M). Under the above-mentioned conditions (h=2.46 mm, T=1135 K, furan conversion 71%) the following reactions play an important role in the formation of ketene (C_2H_2O): C_3H_6+O=C_2H_2O+H+CH_3, C_3H_3+O_2=C_2H_2O+CHO, and iC_4H_3+O_2=C_2H_2O+CHCO. Note that, for a higher temperature and at a higher distance, i.e. h=3.2 mm and T=1828 K, ketene is mainly formed through the unimolecular decomposition of furan (furan=C_2H_2+C_2H_2O). The better match of the predictions for ketene is a clear improvement over the previous model [19]. DME (C_2H_6O) is

25

formed through a combination of CH_3O and CH_3 radicals and mainly consumed by H-abstractions. Propanal and acetone (C_3H_6O) are mainly formed through the reactions CH_3+CH_2CHO and CH_3+CH_3CO, respectively, and then mainly consumed by H-abstractions. Phenol (C_6H_6O) is mainly formed through the combination of the H-atom and the phenoxy radical ($C_6H_5O\#$) which results from the reaction of benzene with an O-atom or of the phenyl radical (C_6H_5) with O_2.

In the stoichiometric furan flame, the same reactions are involved in the consumption of furan as in the rich flame with some differences in their respective importance. Indeed, when the equivalence ratio decreases, the importance of reactions involving oxygenated radicals such as OH radicals or O-atoms is slightly enhanced, while that of reactions involving non-oxygenated radicals such as H-atoms or CH_3 radicals is inhibited. For example, the contribution of the OH-addition to the C=C double bond (forming C_2H_3CHO and the CHO radical) to the fuel consumption increases from ~15% to ~30% when going from fuel-rich to stoichiometric conditions. The mole fractions of C_2H_3CHO (acrolein) and CHO radical have consequently higher values in the stoichiometric flame (see Table 2). Similarly, the contribution of H-abstractions by OH and O to the fuel consumption becomes more important in the stoichiometric flame (~6%, compared to ~3% in the fuel-rich flame). Furthermore, fuel consumption by H-addition at the C2 position decreases with decreasing equivalence ratio (~73% and ~55% at ϕ=1.7 and 1.0, respectively). Fuel consumption by H-addition at the C3 position presents a similar picture (~3% in the fuel-rich flame and ~1.3% in the stoichiometric flame). Therefore, the mole fraction of products yielded by these H-addition channels, such as C_2H_2, is lower in the stoichiometric flame. Overall, a decrease of equivalence ratio from ϕ=1.7 to ϕ=1.0 favors the formation of oxygenated intermediates and inhibits the formation of hydrocarbon intermediates. Thus, the mole fractions of most oxygenated intermediates reach

slightly or significantly higher levels in the stoichiometric flame than in the fuel-rich flame (except for C_2H_6O and C_6H_6O), as shown in Table 2.

6. Summary and conclusion

New experimental and kinetic modeling results have been examined to analyze the chemical structures of two low-pressure premixed furan flames using molecular-beam mass spectrometry and gas chromatography. In this work, mole fraction profiles of about 50 species were measured in two flat furan flames of equivalence ratios ϕ=1.0 and 1.7. It should be noted that the coupling of the information from the GC and EI-MBMS information was very valuable to unambiguously identify the respective isomers for the evaluation of the MBMS data, which could then often be done using the cross section for the dominant isomer. Also, the comparison of both sets of independent quantitative measurements, if only for a selection of stable species, lends additional credibility to the experimental results, especially in situations where both are in good agreement but deviate from the respective simulations. A single kinetic model was used to predict the flame structure of the three fuels: furan (this paper), 2-methylfuran (Part II, [21]), and 2,5-dimethylfuran (Part III, [22]). Simulations were performed with a kinetic model for DMF combustion, recently published by Sirjean et al. [23], with modifications in its furan sub-mechanism and in the H-atom addition processes, and these new routes were found to be important under flame conditions. Perturbed temperature profiles were used as input parameters for the simulation. These profiles were derived directly from the mass spectrometry experiments and calibrated by mid-infrared absorption spectroscopy of CO and CO_2 using a pulsed quantum cascade laser. Good general agreement between experimental and modeling results for the major combustion products as well as for many intermediate species was obtained. This good agreement is valid for profile shapes as well as for the quantitative mole fraction results within experimental uncertainty.

In this study, the simulation performed using the model of Tian et al. [19] is also presented for comparison with the present model. Results show that the present model leads to better results for some species, due to the addition of some reaction pathways of furan as well as to the use of more recent reaction bases for the C_0-C_2 species. Overall, the improvement of our mechanism can be seen in both furan flames.

Finally, a detailed analysis of the reaction pathways was performed based on the detailed mechanism. Furan is mainly consumed by H-addition on the C2 position of furan (the carbon atom bound to the oxygen atom) to form the dihydrofuryl-3 radical (C_4H_5O-3). The second important channel of consumption of furan is the OH-addition on the C-C bond forming acrolein (C_3H_4O) and the CHO radical.

Acknowledgments

Statement about contributions of authors

The EI-MBMS measurements were performed by CT, LST, DL, and DF; they also, with contributions by PO, evaluated the data. PN, JK, and AL performed the temperature measurements. GC measurements and their evaluation were done by LST and PAG with some contributions of DF. Model development and simulations were performed by PAG, BS, LST,

and RF. KKH and FBL directed the work and structured the research and discussions as well as the manuscript writing.

References

[1]   K. Kohse-Höinghaus, P. Oßwald, T.A. Cool, T. Kasper, N. Hansen, F. Qi, C.K. Westbrook, P.R. Westmoreland, Angew. Chem. Int. Ed. 49 (2010) 3572–3597.

[2]   F. Battin-Leclerc, E. Blurock, R. Bounaceur, R. Fournet, P.-A. Glaude, O. Herbinet, B. Sirjean, V. Warth, Chem. Soc. Rev. 40 (2011) 4762–4782.

[3]   Y. Román-Leshkov, C.J. Barrett, Z.Y. Liu, J.A. Dumesic, Nature 447 (2007) 982–986.

[4]   J.-P. Lange, E. van der Heide, J. van Buijtenen, R. Price, ChemSusChem 5 (2012) 150–166.

[5]   L. S. Tran, B. Sirjean, P.-A. Glaude, R. Fournet, F. Battin-Leclerc, Energy 43 (2012) 4–18.

[6]   M.A. Grela, V.T. Amorebieta, A.J. Colussi, J. Phys. Chem. 89 (1985) 38–41.

[7]   A. Lifshitz, M. Bidani, S. Bidani, J. Phys. Chem. 90 (1986) 5373–5377.

[8]   A. Lifshitz, C. Tamburu, R. Shashua, J. Phys. Chem. A 101 (1997) 1018–1029.

[9]   A. Lifshitz, C. Tamburu, R. Shashua, J. Phys. Chem. A 102 (1998) 10655–10670.

[10]   D. Fulle, A. Dib, J.H. Kiefer, Q. Zahng, J. Yao, R.D. Kern, J. Phys. Chem. A 102 (1998) 7480–7486.

[11]   F. Guarneri, E. Ikeda, J.C. Mackie, Energy Fuels 15 (2001) 743–750.

[12]   C.F. Cullis, A.C. Norris, Carbon 10 (1972) 525–537.

[13]   P.P. Organ, J.C. Mackie, J. Chem. Soc. Faraday Trans. 87 (1991) 815–823.

[14]   N.R. Hore, D.K. Russell, New J. Chem. 28 (2004) 606–613.

[15]   A. Vasiliou, M.R. Nimlos, J.W. Daily, G.B. Ellison, J. Phys. Chem. A 113 (2009) 8540–8547.

[16]   R. Liu, X. Zhou, L. Zhai, J. Comput. Chem. 19 (1998) 240–249.

[17] R. Liu, X. Zhou, T. Zuo, Chem. Phys. Lett. 325 (2000) 457–464.

[18] K. Sendt, G.B. Bacskay, J.C. Mackie, J. Phys. Chem. A 104 (2000) 1861–1875.

[19] Z. Tian, T. Yuan, R. Fournet, P.-A. Glaude, B. Sirjean, F. Battin-Leclerc, K. Zhang, F. Qi, Combust. Flame 158 (2011) 756–773.

[20] L. Wei, C. Tang, X. Man, X. Jiang, Z. Huang, Energy Fuels 26 (2012) 2075–2081.

[21] L.-S. Tran, C. Togbé, D. Liu, D. Felsmann, P. Oßwald, P.-A. Glaude, B. Sirjean, R. Fournet, F. Battin-Leclerc, K. Kohse-Höinghaus, Combust. Flame (2013), submitted for publication.

[22] C. Togbé, L.-S. Tran, D. Liu, D. Felsmann, P. Oßwald, P.-A. Glaude, B. Sirjean, R. Fournet, F. Battin-Leclerc, K. Kohse-Höinghaus, Combust. Flame (2013), submitted for publication.

[23] B. Sirjean, R. Fournet, P.-A. Glaude, F. Battin-Leclerc, W. Wang, M.A. Oehlschlaeger, J. Phys. Chem. A 117 (2013) 1371–1392.

[24] B. Sirjean, R. Fournet, Proc. Combust. Inst. 34 (2013) 241–249.

[25] B. Sirjean, R. Fournet, Phys. Chem. Chem. Phys. 15 (2013) 596–611.

[26] B. Sirjean, R. Fournet, J. Phys. Chem. A 116 (2012) 6675–6684.

[27] U. Struckmeier, A. Lucassen, N. Hansen, T. Wada, N. Peters, K. Kohse-Höinghaus, Combust. Flame 157 (2010) 1966–1975.

[28] P. Oßwald, H. Güldenberg, K. Kohse-Höinghaus, B. Yang, T. Yuan, F. Qi, Combust. Flame 158 (2011) 2–15.

[29] A. Lucassen, N. Labbe, P.R. Westmoreland, K. Kohse-Höinghaus, Combust. Flame 158 (2011) 1647–1666.

[30] M. Schenk, L. Leon, K. Moshammer, P. Oßwald, T. Zeuch, L. Seidel, F. Mauss, K. Kohse-Höinghaus, Combust. Flame 160 (2013) 487–503.

[31]   E. Pousse, P.A. Glaude, R. Fournet, F. Battin-Leclerc, Combust. Flame 156 (2009) 954–974.

[32]   S.G. Lias, J.E. Bartmess, J.F. Liebman, J.L. Holmes, R.D. Levin, W.G. Mallard, S.A. Kafafi, "Ion Energetics Data" in NIST Chemistry WebBook, NIST Standard Reference Database Number 69, Eds. P.J. Linstrom and W.G. Mallard, National Institute of Standards and Technology, Gaithersburg MD, 20899, http://webbook.nist.gov

[33]   J.C. Biordi, Prog. Energy Combust. Sci. 3 (1977) 151–173.

[34]   C.J. Dasch, Appl. Opt. 31 (1992) 1146–1152.

[35]   R. Villarreal, P.L. Varghese, Appl. Opt. 44 (2005) 6786–6795.

[36]   L.S. Rothman, I.E. Gordon, R.J. Barber, H. Dothe, R.R. Gamache, A. Goldman, V.I. Perevalov, S.A. Tashkun, J. Tennyson, J. Quant. Spectrosc. Radiat. Transfer 111 (2010) 2139–2150.

[37]   C. Morley, Gaseq V.063, Program for thermodynamic gas equation, 1999.

[38]   R.J. Kee, F.M. Rupley, J.A. Miller, CHEMKIN II: A Fortran Chemical Kinetics Package for the Analysis of Gas-Phase Chemical Kinetics, Report No. SAND89-8009, Sandia National Laboratories, 1989.

[39]   S.M. Sarathy, S. Vranckx, K. Yasunaga, M. Mehl, P. Oßwald, W.K. Metcalfe, C.K. Westbrook, W.J. Pitz, K. Kohse-Höinghaus, R.X. Fernandes, H.J. Curran, Combust. Flame 159 (2012) 2028–2055.

[40]   R. Bounaceur, I. da Costa, R. Fournet, F. Billaud, F. Battin-Leclerc, Int. J. Chem. Kinet. 37 (2005) 25–49.

[41]   H.A. Gueniche, P.A. Glaude, R. Fournet, F. Battin-Leclerc, Combust. Flame 151 (2007) 245–261.

[42]   B. Husson, R. Bounaceur, K. Tanaka, M. Ferrari, O. Herbinet, P.A. Glaude, R. Fournet, F. Battin-Leclerc, M. Crochet, G. Vanhove, R. Minetti, C.J. Tobin, K. Yasunaga, J.M.

Simmie, H.J. Curran, T. Niass, O. Mathieu, S.S. Ahmed, Combust. Flame 159 (2012) 1399–1416.

[43]   J.A. Montgomery, Jr., M.J. Frisch, J.W. Ochterski, G.A. Petersson, J. Chem. Phys. 110 (1999) 2822–2827.

[44]   Gaussian 09, Revision B.01, M.J. Frisch, G.W. Trucks, H.B. Schlegel, G.E. Scuseria, M.A. Robb, J.R. Cheeseman, G. Scalmani, V. Barone, B. Mennucci, G.A. Petersson, H. Nakatsuji, M. Caricato, X. Li, H.P. Hratchian, A.F. Izmaylov, J. Bloino, G. Zheng, J.L. Sonnenberg, M. Hada, M. Ehara, K. Toyota, R. Fukuda, J. Hasegawa, M. Ishida, T. Nakajima, Y. Honda, O. Kitao, H. Nakai, T. Vreven, J.A. Montgomery, Jr., J.E. Peralta, F. Ogliaro, M. Bearpark, J.J. Heyd, E. Brothers, K.N. Kudin, V.N. Staroverov, R. Kobayashi, J. Normand, K. Raghavachari, A. Rendell, J.C. Burant, S.S. Iyengar, J. Tomasi, M. Cossi, N. Rega, J.M. Millam, M. Klene, J.E. Knox, J.B. Cross, V. Bakken, C. Adamo, J. Jaramillo, R. Gomperts, R.E. Stratmann, O. Yazyev, A.J. Austin, R. Cammi, C. Pomelli, J.W. Ochterski, R.L. Martin, K. Morokuma, V.G. Zakrzewski, G.A. Voth, P. Salvador, J.J. Dannenberg, S. Dapprich, A.D. Daniels, Ö. Farkas, J.B. Foresman, J.V. Ortiz, J. Cioslowski, D.J. Fox, Gaussian, Inc., Wallingford CT, 2009.

[45]   I.R. Slagle, J.R. Bernhardt, D. Gutman, Proc. Combust. Inst. 22 (1989) 953–962.

[46]   K.N. Joshipura, M. Vinodkumar, U.M. Patel, J. Phys. B: At. Mol. Opt. Phys. 34 (2001) 509–519.

[47]   O.J. Orient, S.K. Srivastava, J. Phys. B: At. Mol. Opt. Phys. 20 (1987) 3923–3936.

[48]   W.L. Fitch, A.D. Sauter, Anal. Chem. 55 (1983) 832–835.

[49]   Y.-K. Kim, K.K. Irikura, M.E. Rudd, M.A. Ali, P.M. Stone, J.S. Coursey, R.A. Dragoset, A.R. Kishore, K.J. Olsen, A.M. Sansonetti, G.G. Wiersma, D.S. Zucker, M.A. Zucker, Electron-Impact Cross Sections for Ionization and Excitation, http://physics.nist.gov/PhysRefData/Ionization/Xsection.html

[50] H. Nishimura, H. Tawara, J. Phys. B: At. Mol. Opt. Phys. 27 (1994) 2063–2074.

Table 1

Flow conditions for furan flames; SLM: Standard liter per minute.

	ϕ	Burner diameter (mm)	Gas flow (SLM)			Pressure (mbar)	C/O ratio	Dilution	Flow velocity at T=333 K[#] (cm s^{-1})
			Furan	O$_2$	Ar				
Bielefeld	1.0	64	0.42	1.87	2.28	20	0.40	50%	146
	1.7	64	0.63	1.65	2.28	40	0.64	50%	73
Nancy	1.7	60	0.55	1.45	2.00	40	0.64	50%	73

[#] The flow velocity is referred to the temperature of the burner surface (cooling water).

Table 2

Intermediate species identification with EI-MBMS in furan experiments. *M*: nominal mass, *E*: electron energy, *IP*: ionization threshold, *h*: position of maximum, x_{max}: peak mole fraction, ϕ: equivalence ratio. Calibration methods: RICS (of reference species in parenthesis), convolution (of energy distribution and ionization cross section) or direct (cold gas calibration).

Species	M	E (eV)	IP (eV)	Calibrated as	Calibration method	Ref	φ=1.0		φ=1.7	
							h (mm)	x_{max}	h (mm)	x_{max}
CH$_3$	15	10.5	9.84	Methyl	RICS (CH$_4$)	[46]	3.0	1.14E-03	3.0	1.49E-03
CH$_4$	16	12.0	12.61	Methane	Direct	[47]	4.0	2.36E-03	3.0	3.30E-03
C$_2$H$_2$	26	12.0	11.40	Acetylene	Direct	[48]	4.0	1.82E-02	3.0	3.49E-02
C$_2$H$_3$	27	10.5	8.25	Vinyl	RICS (C$_2$H$_4$)	[49]	2.2	6.32E-06	2.5	5.77E-06
C$_2$H$_4$	28	11.25	10.51	Ethene	Direct	[50]	3.2	5.69E-03	2.5	6.72E-03
C$_2$H$_5$	29	10.5	8.12	Ethyl	RICS (C$_2$H$_6$)	[49]	2.5	2.69E-05	2.5	2.36E-05
HCO	29	10.5	8.12	Formyl	Convolution	[49]	2.5	7.11E-05	2.0	5.50E-05
C$_2$H$_6$	30	12.0	11.52	Ethane	Direct	[50]	3.0	1.45E-03	2.5	1.98E-03
CH$_2$O	30	11.25	10.88	Formaldehyde	Convolution	[49]	2.5	3.95E-03	2.5	3.84E-03
CH$_4$O	32	11.25	10.23	Methanol	Direct	[50]	2.0	4.92E-04	1.5	4.36E-04
C$_3$H$_3$	39	10.5	8.67	Propargyl	RICS (C$_3$H$_6$)	[49]	3.2	3.72E-05	3.0	1.04E-04
C$_3$H$_4$	40	11.25	10.36	Propyne	RICS (C$_3$H$_6$)	[49]	3.0	1.82E-03	3.0	2.96E-03
C$_3$H$_5$	41	10.5	8.13	Allyl	RICS (C$_3$H$_6$)	[49]	3.0	1.52E-04	3,0	1.51E-04
C$_2$H$_2$O	42	10.5	9.62	Ketene	Convolution	RICS (C$_2$H$_6$O)	3.5	3.61E-04	3.0	3.58E-04
C$_3$H$_6$	42	10.5	9.73	Propene	Direct	[50]	2.7	1.43E-03	2.5	1.11E-03
C$_2$H$_4$O	44	11.25	10.23	Acetaldehyde	Direct	[48]	2.5	3.74E-03	2.0	3.18E-03
C$_2$H$_6$O	46	10.5	10.02	Dimethylether	Direct	[48]	2.2	2.39E-05	1.5	3.90E-05
C$_4$H$_2$	50	11.25	10.17	1,3-Butadiyne	Convolution	[49]	4.0	1.34E-04	4.0	1.08E-03
C$_4$H$_4$	52	10.5	9.58	1-Butene-3-yne	Convolution	[49]	3.5	1.63E-04	3.0	4.82E-04
C$_4$H$_5$	53	10.5	7.97	But-2-yn-1-yl	Convolution	RICS (C$_4$H$_6$)	3.0	2.38E-06	3.0	5.33E-06
C$_4$H$_6$	54	10.5	9.07	1,3-Butadiene	Convolution	[49]	3.0	2.48E-04	2.5	4.56E-04

Species	M	E (eV)	IP (eV)	Calibrated as	Calibration method	Ref	φ=1.0		φ=1.7	
							h (mm)	x_{max}	h (mm)	x_{max}
C_4H_7	55	10.5	7.40	But-3-en-1-yl	RICS (1-C_4H_8)	[49]	2.5	7.75E-06	2.5	1.40E-05
C_4H_8	56	10.5	9.55	1-Butene	Direct	[50]	2.2	5.10E-04	2.0	6.43E-04
C_3H_4O	56	11.25	10.11	Acrolein	RICS (C_3H_6O)	[48]	2.5	2.75E-03	2.0	2.45E-03
C_3H_6O	58	10.5	9.96	Propanal	Convolution	[48]	2.0	8.60E-04	2.0	4.17E-04
C_5H_4	64	10.5	9.50	1,3-Pentadiyne	RICS (C_5H_8)	[48]	3.5	5.93E-06	3.0	2.82E-05
C_5H_6	66	10.5	8.57	1,3-Cyclopentadiene	RICS (C_5H_8)	[48]	3.0	4.92E-05	2.5	1.01E-04
C_4H_6O	70	10.5	9.75	2-Butenal	Convolution	RICS (butanal)	1.7	3.97E-04	1.0	2.92E-04
C_5H_{10}	70	10.5	9.04	2-Pentene	RICS (C_5H_8)	[48]	2.2	1.30E-05	2.0	2.47E-05
C_4H_8O	72	10.5	9.71	Isobutanal	Convolution	RICS (butanal)	2.0	1.05E-04	1.5	1.03E-04
C_6H_2	74	10.5	9.50	Triacetylene	Convolution	[49]	4.0	3.22E-06	3.5	3.66E-05
C_6H_4	76	10.5	9.03	Benzyne	Convolution	RICS (C_6H_2)	3.7	1.74E-06	3.5	1.19E-05
C_6H_6	78	10.5	9.24	Benzene	Direct	[49]	3.0	4.23E-05	3.0	1.31E-04
C_5H_8O	84	10.5	8.70	2,5-Dihydro-2MF	Convolution	RICS (furan)	2.0	2.05E-05	1.5	1.07E-05
C_7H_8	92	10.5	8.82	Toluene	Convolution	RICS (C_6H_6)	3.2	2.98E-06	3.0	9.63E-06
C_6H_6O	94	10.5	8.49	Phenol	Convolution	RICS (C_6H_6)	3.2	6.15E-06	2.5	9.70E-06
C_6H_8O	96	10.5	7.80	2,5-Dimethylfuran	Convolution	RICS (furan)	2.5	5.80E-06	2.0	4.98E-06

Table 3

Comparison of maximum mole fractions (GC/MBMS/Model) for some intermediates in the furan/O_2/Ar flame, ϕ=1.7.

Formula	Species	x_{max} (GC)	x_{max} (Model)	x_{max} (MBMS)
C_2H_2	Acetylene	3.01E-02	2.99E-02	3.49E-02
C_2H_4	Ethene	9.98E-03	3.40E-03	6.72E-03
C_2H_6	Ethane	2.89E-03	1.90E-03	1.98E-03
C_3H_4	Propyne	1.37E-03	0.47E-03	2.96E-03
	Allene	3.78E-04	4.30E-04	
C_3H_6	Propene	1.37E-03	3.50E-03	1.11E-03
C_4H_4	1-Butene-3-yne	6.01E-04	4.50E-04	4.82E-04
C_4H_6	1,3-Butadiene	4.90E-04	0.81E-04	4.56E-04
	1,2-Butadiene	3.84E-05	3.61E-05	
	2-Butyne	1.53E-05	0.50E-05	
C_4H_8	1-Butene	2.79E-04	3.91E-04	6.43E-04
	2-Butene	7.28E-05	2.70E-05	
C_5H_6	1,3-Cyclopentadiene	8.46E-05	1.10E-05	10.10E-05
	1-Pentene-3-yne	1.06E-05	a	
C_5H_{10}	2-Pentene	3.32E-05	2.23E-05	2.47E-05
	3-Methyl-1-butene	1.28E-05		
	1-Pentene	3.84E-06	0.10E-06	
C_6H_6	Benzene	1.15E-04	0.90E-04	1.30E-04
C_7H_8	Toluene	11.6E-06	50.3E-06	9.63E-06
C_2H_4O	Acetaldehyde	4.23E-03	1.10E-03	3.18E-03
	Ethylene oxide	3.37E-06	9.50E-05	
C_2H_6O	DME	4.61E-05	4.00E-05	3.90E-05
	Ethanol	b	a	
C_3H_4O	Acrolein (Propenal)	c	3.31E-03	2.45E-03
C_3H_6O	Propanal	9.53E-05	2.44E-04	5.89E-04
	Acetone	2.31E-05	0.22E-06	
C_4H_6O	2-Butenal	7.38E-05	a	29.20E-05
	2-Butenone	3.38E-05	a	
	Isobutenal	1.64E-05	a	
	2,3-Dihydrofuran	2.78E-06	5.09E-04	
C_4H_8O	Isobutanal	8.00E-05	a	12.80E-05
	2-Butanone	3.66E-06	a	
C_5H_6O	2-Methylfuran	4.32E-05	2.04E-05	8.89E-05
	3-Methylfuran	1.69E-05	a	

a: not available ; b: not detected; c: identified, but not quantified.

Table 4

Calculated rate coefficients of reactions R231, R234, and R235 in the format $A \times T^n \times exp(-E/RT)$, (k units: cm^3, mol, s^{-1}, kcal).

No.	Reactions	A	n	E
R231	CHCHCH$_2$CHO = CO + C$_3$H$_5$-Y	1.40E+06	1.326	6.19
R234	CH$_2$CHCHCHO = CH$_3$CHCHCO	1.81E+09	0.985	28.8
R235	CH$_3$CHCHCO = CO + C$_3$H$_5$-s	1.43E+15	0.115	26.6

Table 5

Structure and nomenclature of some species involved in the detailed mechanism of the furan oxidation.
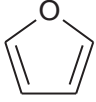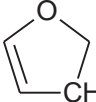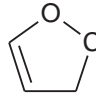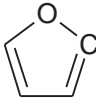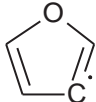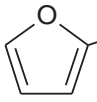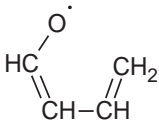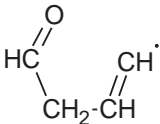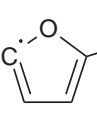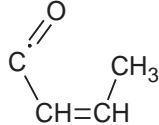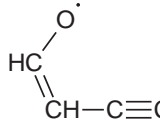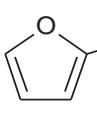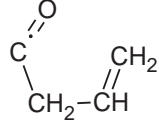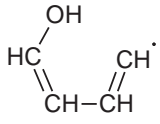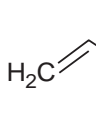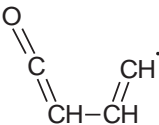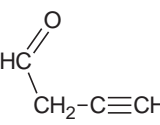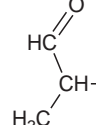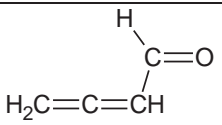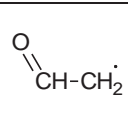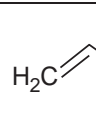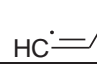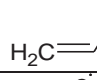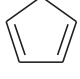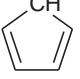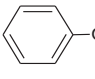
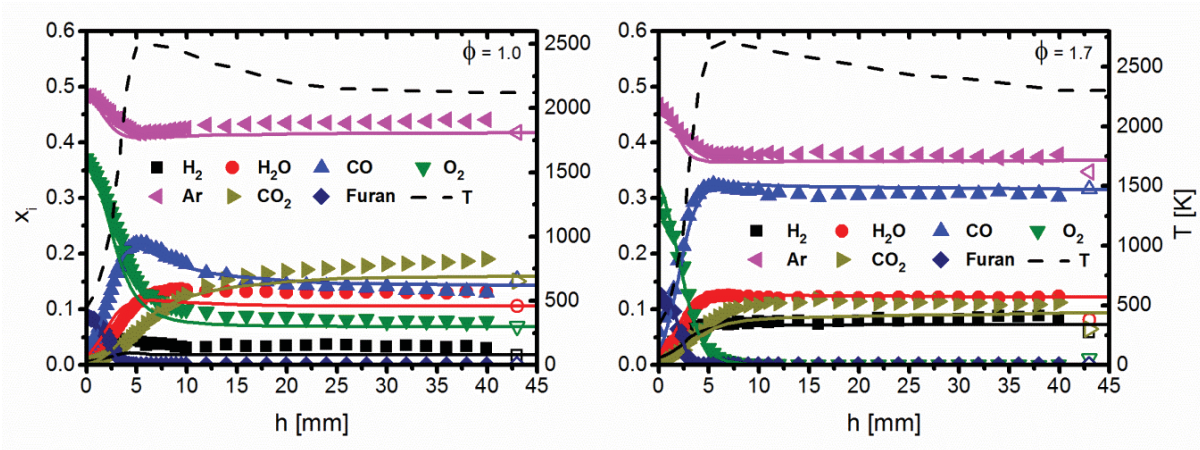| Species	Name	Species	Name	Species	Name
	Furan		C_4H_5O-3		C_4H_5O-2
	Furyl-2		Furyl-3		MF
	$CH_2CHCHCHO$		$CHCHCH_2CHO$		M5F-2yl
	$CH_3CHCHCO$		$CHCCHCHO$		$FurylCH_2$
	CH_2CHCH_2CO		$CHCHCHCHOH$		CH_2CHCO
	$CHCHCHCO$		$CHCCH_2CHO$		C_5H_6O
	$CH_2CCHCHO$		CH_2CHO		C_2H_3CHO (C_3H_4O)
$H_3C-CH-C{\equiv}CH$	C_4H_5-1s	$O{=}C{=}CH$	CHCO		C_3H_5-s
$HC{\equiv}C-CH_2$	C_3H_3	$HC{\equiv}C-CH_3$	p-C_3H_4		C_3H_5-Y
$HC{\equiv}C-CH{=}CH_2$	C_4H_4	$HC{\equiv}C-C{\equiv}CH$	C_4H_2		C_6H_5
	1,3-C_5H_6		C_5H_5#		C_6H_5O#

39

Figure captions

Figure 1. Main species mole fraction x_i and temperature T profiles as a function of height above burner h. Symbols: experiment (EI-MBMS), lines: model results. Equilibrium values (open symbols) are indicated at h=43 mm. Perturbed temperature profiles were calibrated by QCL absorption at 25.0 mm; they were used as input parameters for the numerical simulation without any changes.
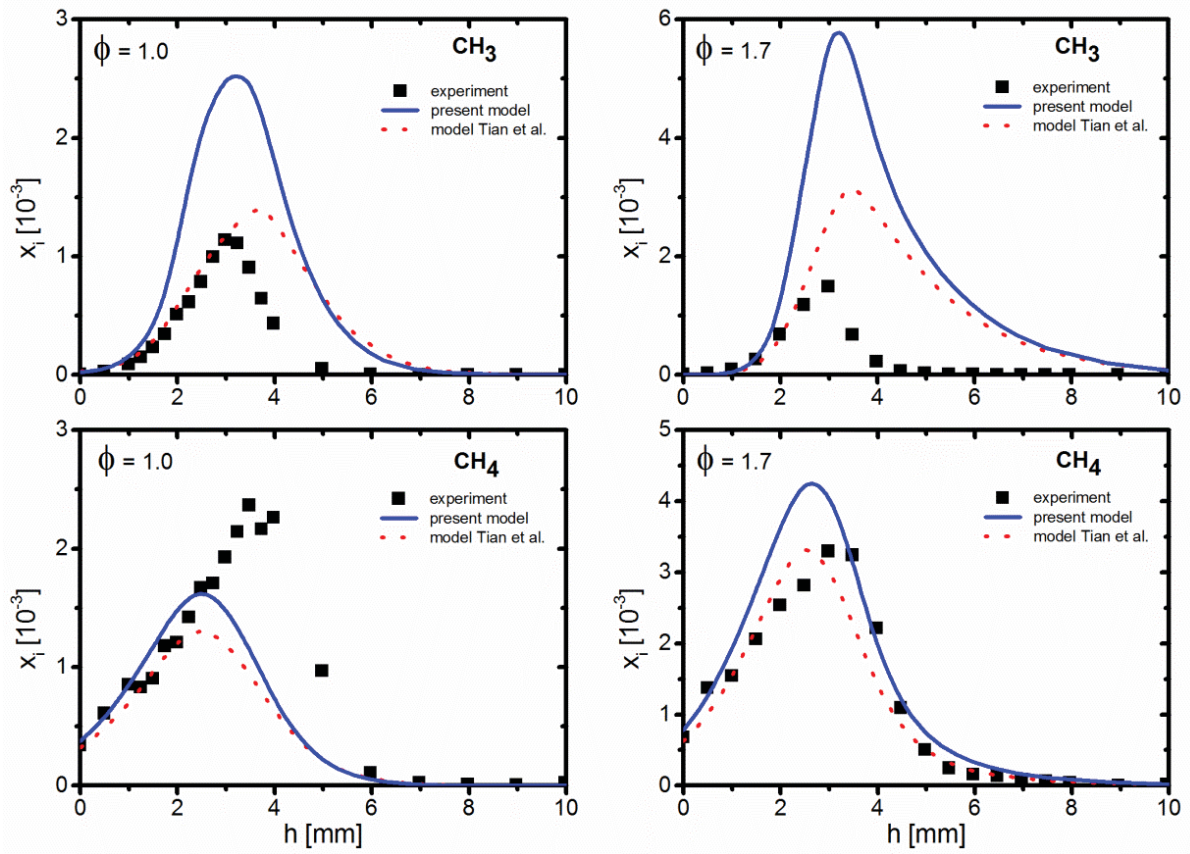
Figure 2. Mole fraction profiles of C_1 species. Symbols: experiment (EI-MBMS); lines: simulation; solid lines: present model, dotted lines: model of Tian et al. [19].

Figure 3. Mole fraction profiles of C_2 species. Symbols: experiment (EI-MBMS); lines: simulation; solid lines: present model, dotted lines: model of Tian et al. [19].

Figure 4. Mole fraction profiles of C_3 species. Symbols: experiment (EI-MBMS); lines: simulation; solid lines: present model, dotted lines: model of Tian et al. [19].

Figure 5. Mole fraction profiles of C_4 species. Symbols: experiment (EI-MBMS); lines: simulation; solid lines: present model, dotted lines: model of Tian et al. [19].

Figure 6. Mole fraction profiles of C_5-C_6 species. Symbols: experiment (EI-MBMS); lines: simulation; solid lines: present model, dotted lines: model of Tian et al. [19], except for C_5H_{10} (simulation data were not available).

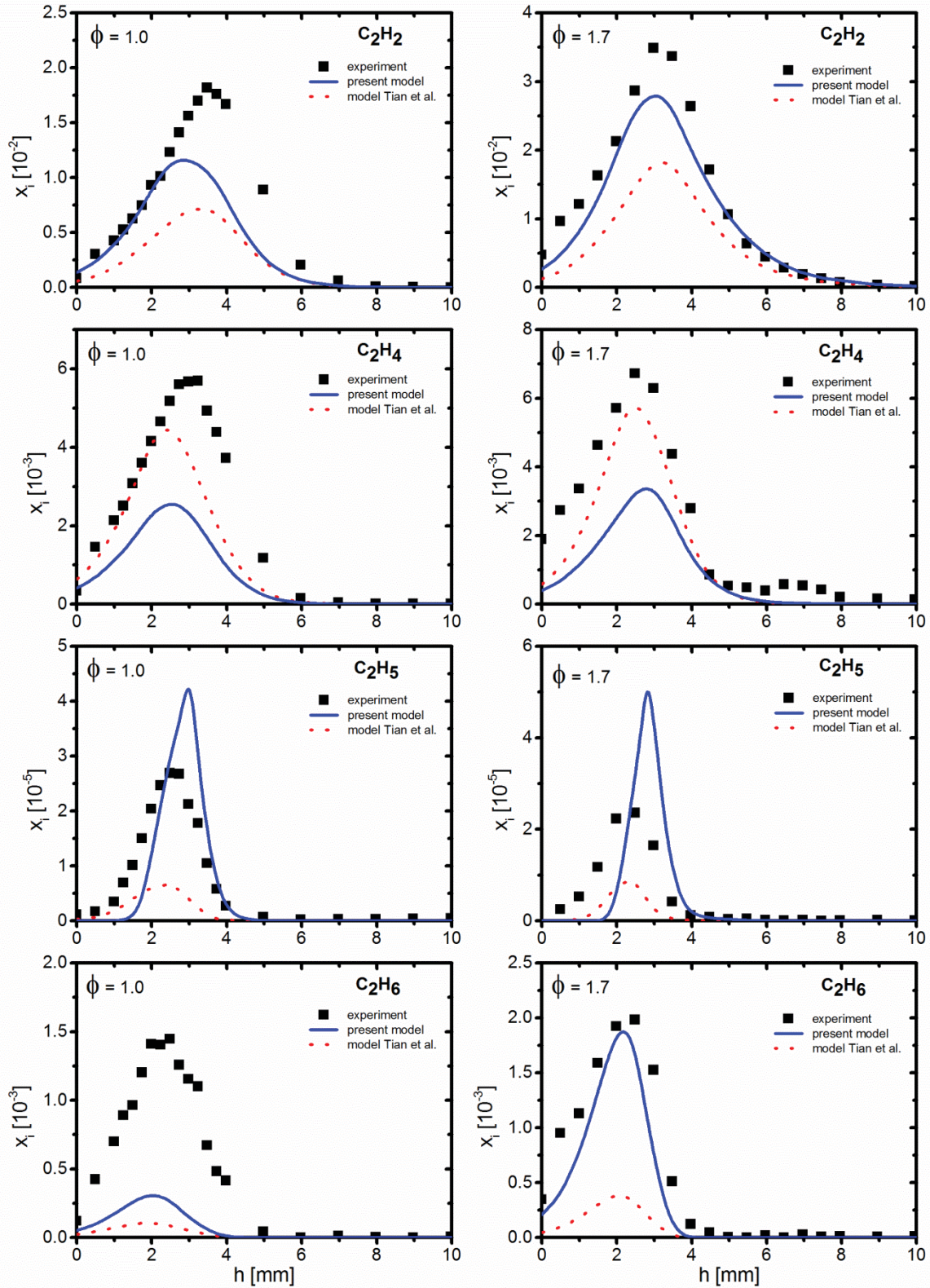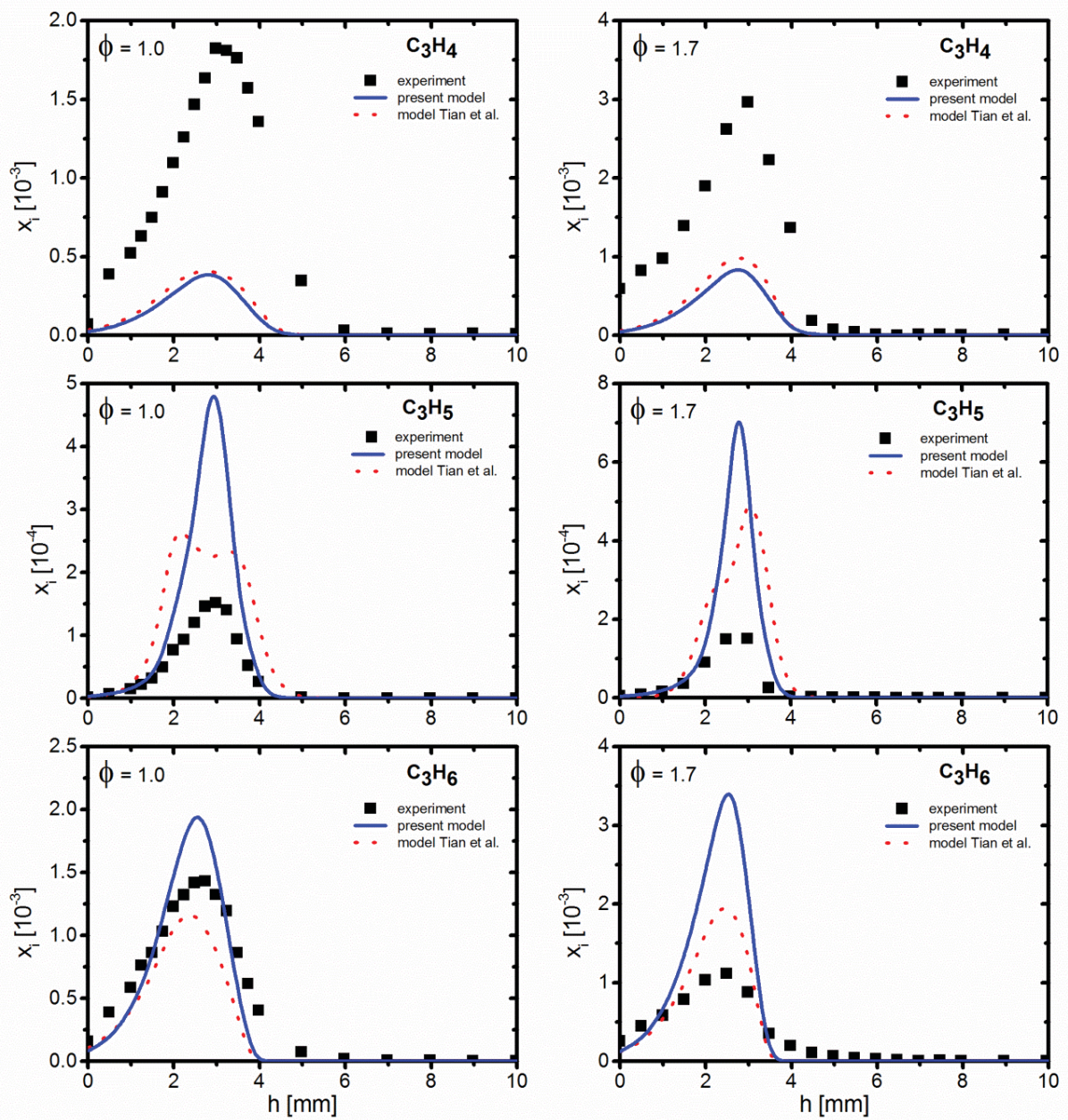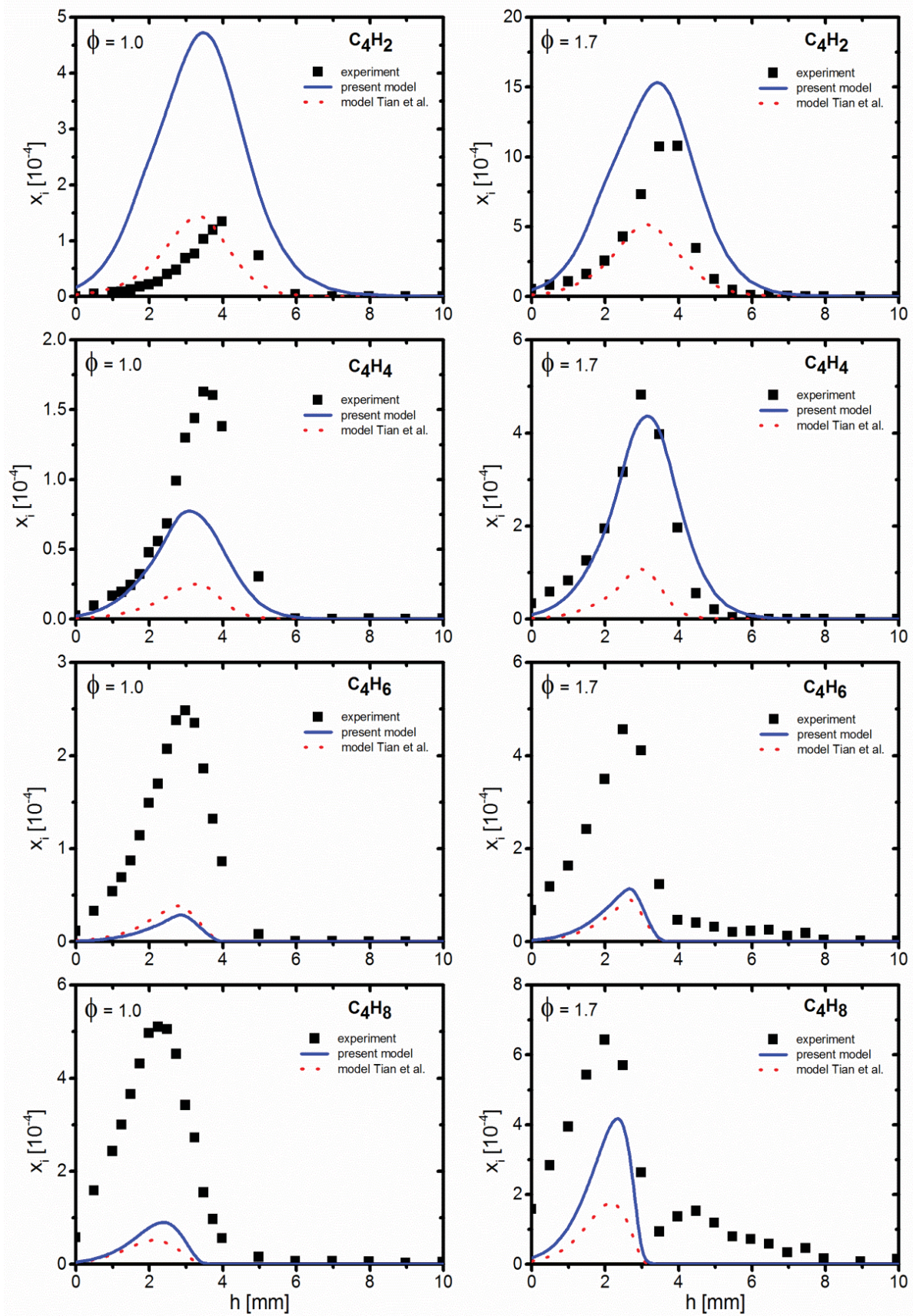**Figure 7.** Mole fraction profiles of C_1-C_2 oxygenated species. Symbols: experiment (EI-MBMS); lines: simulation; solid lines: present model, dotted lines: model of Tian et al. [19], except for C_2H_6O (simulation data were not available).

Figure 8. Selected C_3 and C_6 oxygenated species profiles. Symbols (EI-MBMS): experiment; lines: simulation; solid lines: present model, dotted lines: model of Tian et al. [19].

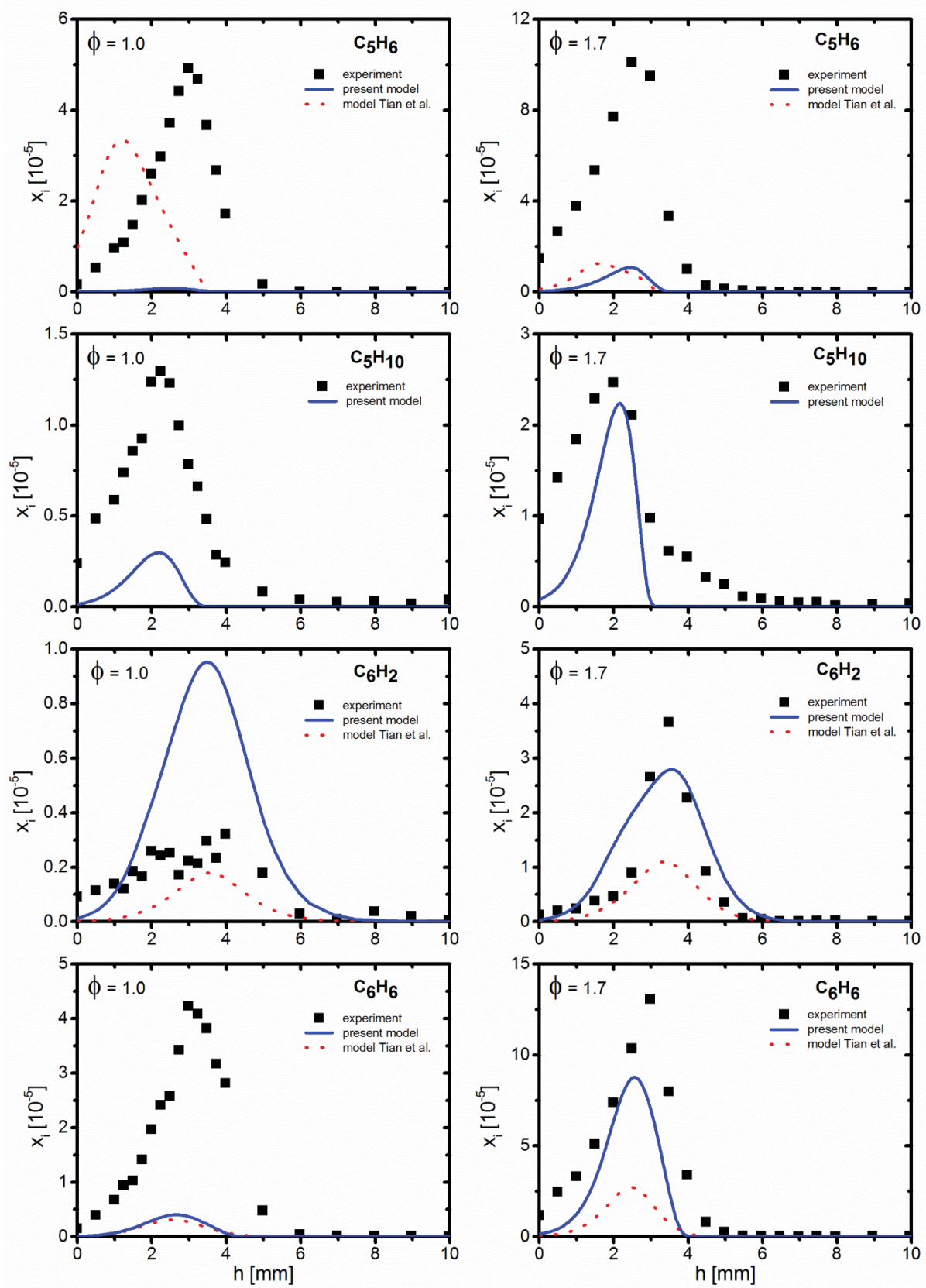**Figure 9.** C_3H_4 isomers (allene and propyne). Mole fraction profiles (sum of C_3H_4) obtained in the MBMS experiment and results of the GC analysis (left), and respective model prediction (right).

Figure 10. C_3H_6O isomers (propanal and acetone). Mole fraction profiles (sum of C_3H_6O) obtained in the MBMS experiment and results of the GC analysis (left), and respective model prediction (right).

Figure 11. Unimolecular decompositions of dihydrofuryl radicals (C_4H_5O-2 and C_4H_5O-3): solid arrows have been considered in the mechanism of Tian et al. [19]; dashed arrows are added in the present study; pathway with cross sign ($\times$) is not considered. Activation energies (kcal mol^{-1}) are in bold. The rate coefficients of reaction R231, R234, and R235 are given in Table 4.

Figure 12. Flow-rate analysis for the consumption of furan in the fuel-rich furan flame (ϕ=1.7) for a distance of 2.46 mm from the burner corresponding to a simulated temperature of 1135 K and 71% conversion of furan. The size of the arrows is proportional to the relative flow rates of consumption of a given species. Reaction pathways in the dashed square have been added in the present study (see Section 4).

Figure 1. Main species mole fraction x_i and temperature T profiles as a function of height above burner h. Symbols: experiment (EI-MBMS), lines: model results. Equilibrium values (open symbols) are indicated at h=43 mm. Perturbed temperature profiles were calibrated by QCL absorption at 25.0 mm; they were used as input parameters for the numerical simulation without any changes.

Figure 2. Mole fraction profiles of C_1 species. Symbols: experiment (EI-MBMS); lines: simulation; solid lines: present model, dotted lines: model of Tian et al. [19].
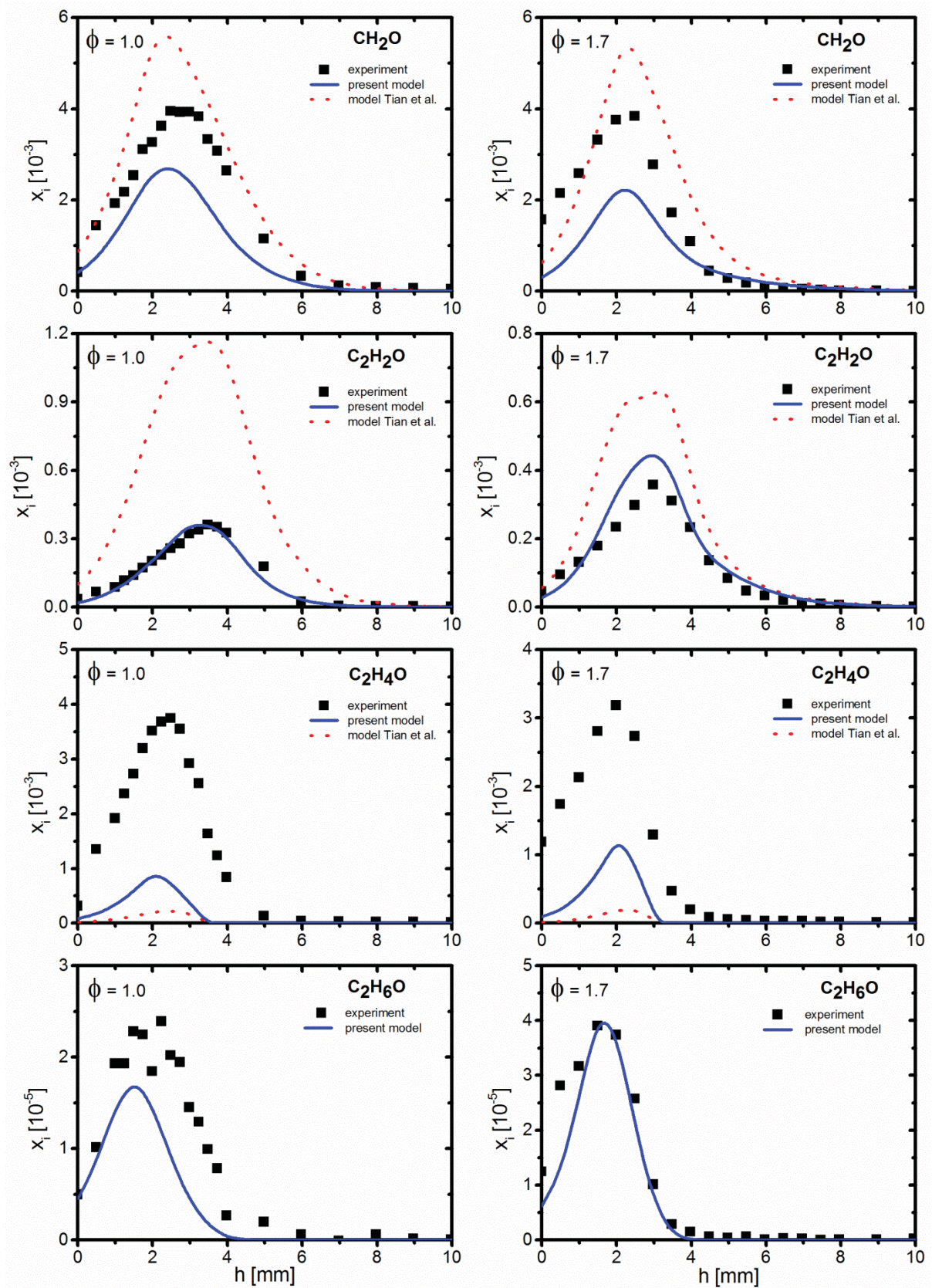
Figure 3. Mole fraction profiles of C_2 species. Symbols: experiment (EI-MBMS); lines: simulation; solid lines: present model, dotted lines: model of Tian et al. [19].

Figure 4. Mole fraction profiles of C_3 species. Symbols: experiment (EI-MBMS); lines: simulation; solid lines: present model, dotted lines: model of Tian et al. [19].

Figure 5. Mole fraction profiles of C_4 species. Symbols: experiment (EI-MBMS); lines: simulation; solid lines: present model, dotted lines: model of Tian et al. [19].

Figure 6. Mole fraction profiles of C_5-C_6 species. Symbols: experiment (EI-MBMS); lines: simulation; solid lines: present model, dotted lines: model of Tian et al. [19], except for C_5H_{10} (simulation data were not available).
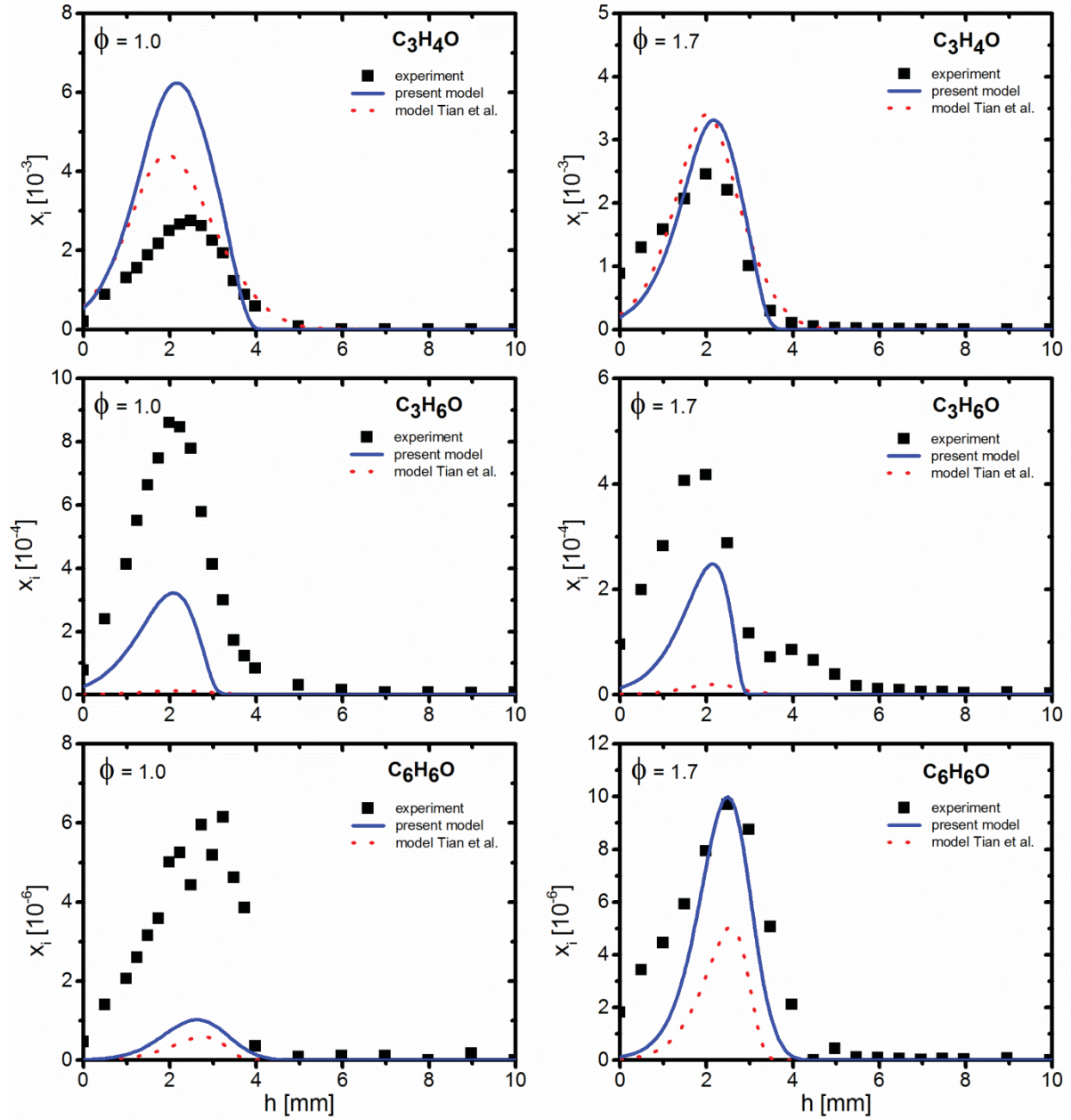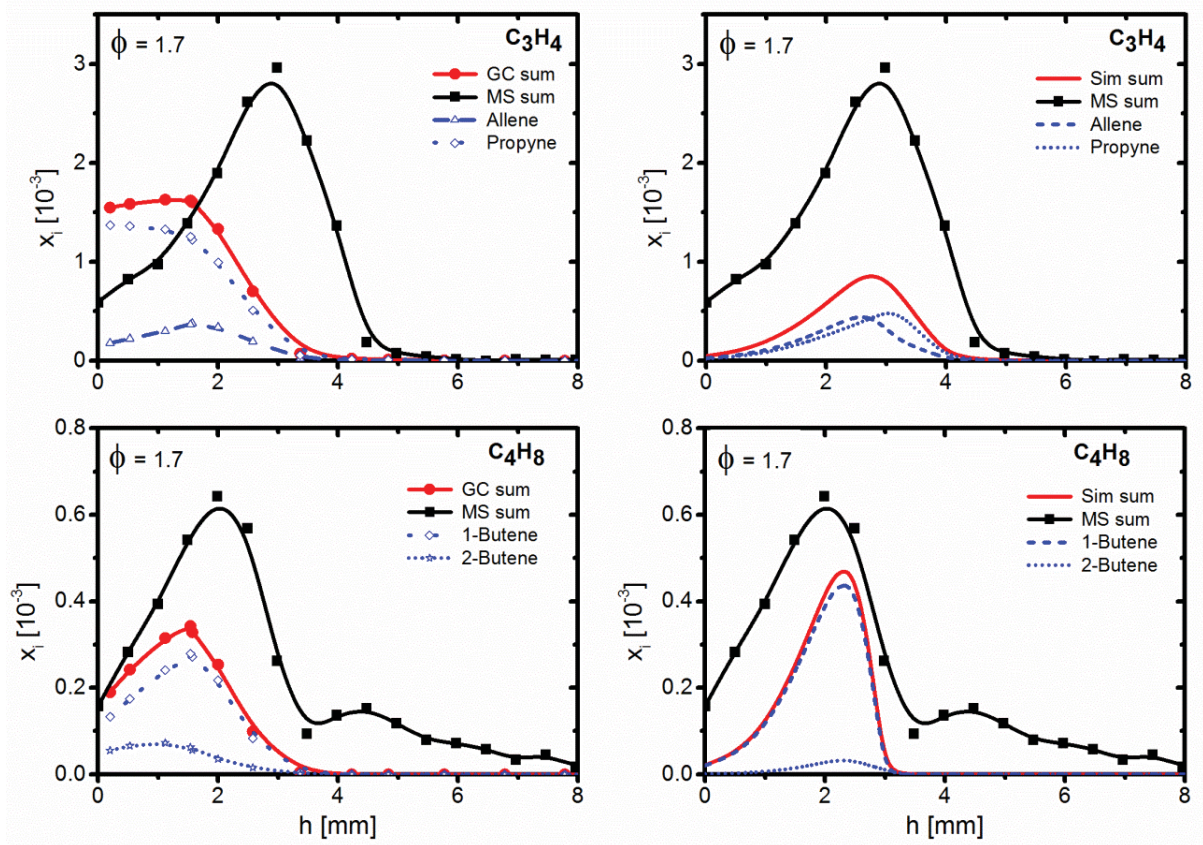
Figure 7. Mole fraction profiles of C_1-C_2 oxygenated species. Symbols: experiment (EI-MBMS); lines: simulation; solid lines: present model, dotted lines: model of Tian et al. [19], except for C_2H_6O (simulation data were not available).

Figure 8. Selected C_3 and C_6 oxygenated species profiles. Symbols: experiment (EI-MBMS); lines: simulation; solid lines: present model, dotted lines: model of Tian et al. [19].

Figure 9. C_3H_4 and C_4H_8 isomers. Mole fraction profiles (sum of C_3H_4 and C_4H_8) obtained in the MBMS experiment and results of the GC analysis (left), and respective model prediction (right).
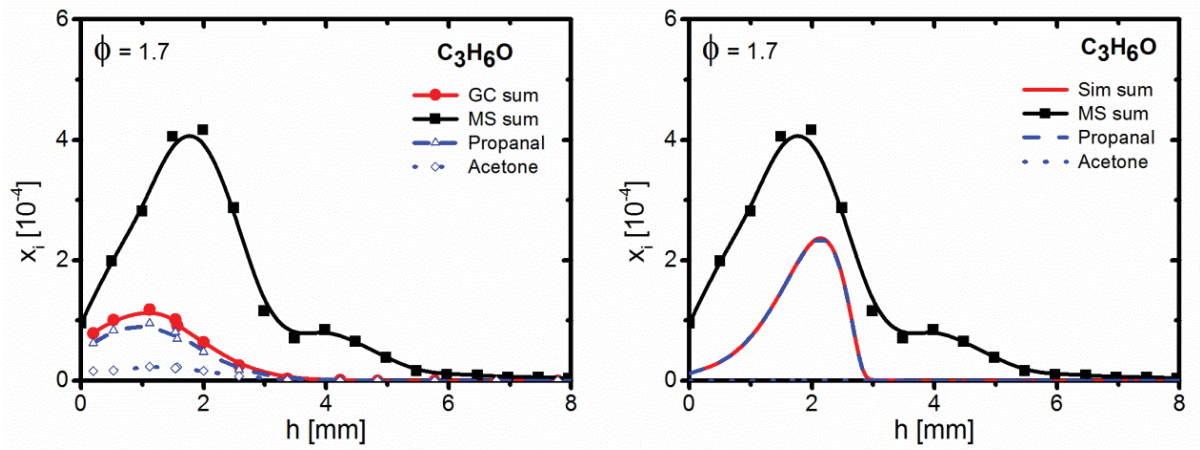
Figure 10. C_3H_6O isomers (propanal and acetone). Mole fraction profiles (sum of C_3H_6O) obtained in the MBMS experiment and results of the GC analysis (left), and respective model prediction (right).
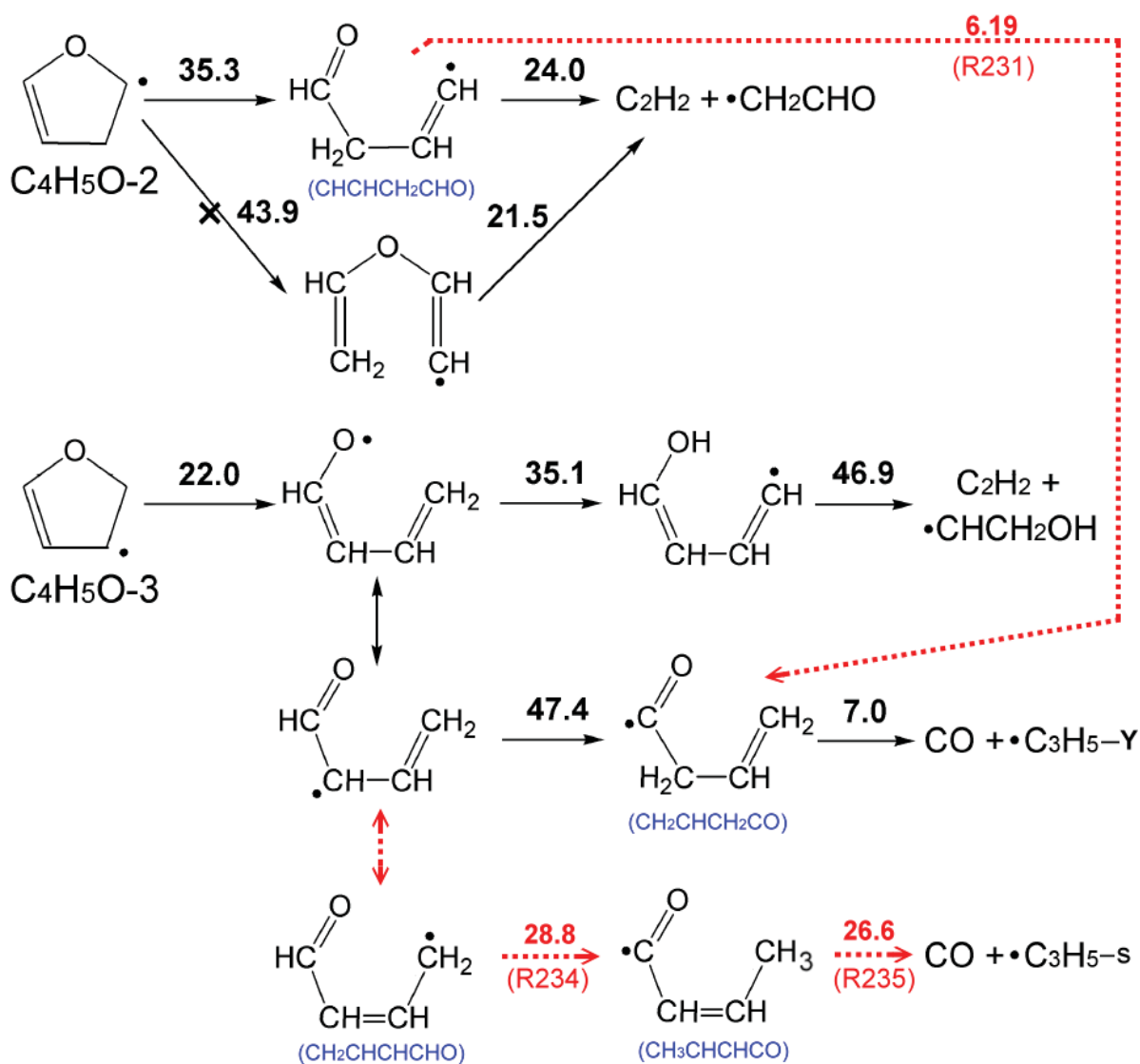
Figure 11. Unimolecular decompositions of dihydrofuryl radicals (C_4H_5O-2 and C_4H_5O-3): solid arrows have been considered in the mechanism of Tian et al. [19]; dashed arrows are added in the present study; pathway with cross sign (×) is not considered. Activation energies (kcal mol^{-1}) are in bold. The rate coefficients of reaction R231, R234, and R235 are given in Table 4.
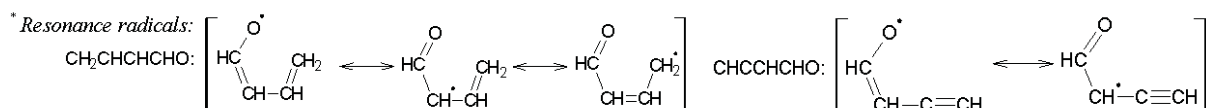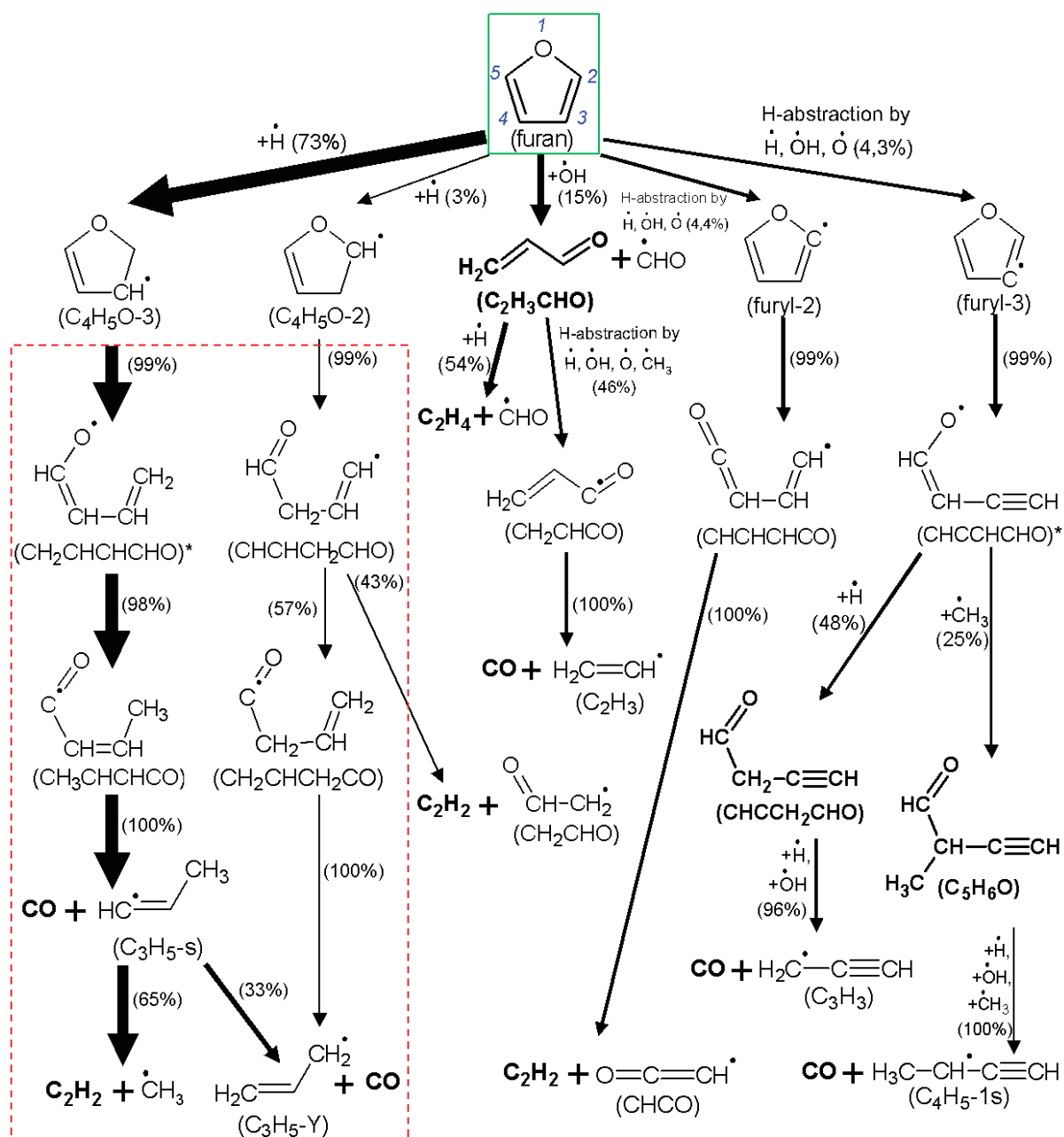
Figure 12. Flow-rate analysis for the consumption of furan in the fuel-rich furan flame (φ=1.7) for a distance of 2.46 mm from the burner corresponding to a simulated temperature of 1135 K and 71% conversion of furan. The size of the arrows is proportional to the relative flow rates of consumption of a given species. Reaction pathways in the dashed square have been added in the present study (see Section 4).